s-Process Abundances in Planetary Nebulae

Brian Sharpee[1], Yong Zhang[2,3], Robert Williams[2], Eric Pellegrini[4], Kenneth Cavagnolo[4], Jack A. Baldwin[4], Mark Phillips[5], and Xiao-Wei Liu[3]

ABSTRACT

The *s*-process should occur in all but the lower mass progenitor stars of planetary nebulae, and this should be reflected in the chemical composition of the gas which is expelled to create the current planetary nebula shell. Weak forbidden emission lines are expected from several *s*-process elements in these shells, and have been searched for and in some cases detected in previous investigations. Here we extend these studies by combining very high signal-to-noise echelle spectra of a sample of PNe with a critical analysis of the identification of the emission lines of Z>30 ions. Emission lines of Br, Kr, Xe, Rb, Ba, and Pb are detected with a reasonable degree of certainty in at least some of the objects studied here, and we also tentatively identify lines from Te and I, each in one object. The strengths of these lines indicate enhancement of *s*-process elements in the central star progenitors, and we determine the abundances of Br, Kr, and Xe, elements for which atomic data relevant for abundance determination have recently become available. As representative elements of the "light" and "heavy" *s*-process peaks Kr and Xe exhibit similar enhancements over solar values, suggesting that PNe progenitors experience substantial neutron exposure.

Subject headings: ISM: abundances — nuclear reactions, nucleosynthesis, abundances — planetary nebulae: general

1. Introduction

As remnants of stars that have evolved through the asymptotic giant branch (AGB) phase, most planetary nebulae (PNe) are believed to consist of material that has undergone nuclear processing in the precursor star via the *s*-process. The analysis of nebular emission from elements that have experienced nucleosynthesis in the parent star provides valuable information for stellar models. However, the detection of emission lines from ions enhanced

[1]SRI International, 333 Ravenswood Ave. Menlo Park, CA 94025, USA

[2]Space Telescope Science Institute, 3700 San Martin Drive, Baltimore, MD 21218, USA

[3]Department of Astronomy, Peking University, Beijing 100871, P. R. China

[4]Department of Physics & Astronomy, Michigan State University, East Lansing, MI 48824, USA

[5]Las Campanas Observatory, Carnegie Observatories, Casilla 601, La Serena, Chile

by the *s*-process has been hampered by their weakness and by uncertainties in the atomic data needed for the analysis, including line wavelengths.

An initial attack on this problem was made a decade ago by Péquignot & Baluteau (1994) (hereafter PB94), who obtained a deep optical spectrum of the high-ionization PN NGC 7027. Using the best atomic data available for the energy levels of the more prominent ionization stages of elements in the fourth and fifth rows of the periodic table, they identified a number of post-Fe peak emission lines in the nebula. From the observed line intensities they concluded that the elements Kr and Xe, the latter normally a predominantly *r*-process element in stars of solar metalicity, were enhanced in NGC 7027 by factors of ∼20 relative to their initial formation abundances, presumably roughly solar. They also detected Ba II and [Br III] emission at intensities indicating that Ba could be enhanced whereas Br might be depleted relative to solar values, subject to uncertainty due to poorly known excitation cross sections.

Dinerstein and collaborators have subsequently pursued the study of *s*-process abundances in PNe through surveys to detect IR fine-structure nebular emission from post-Fe peak ions (Dinerstein 2001; Sterling & Dinerstein 2004) and from far-UV resonance-line absorption by *s*-process elements in the intervening nebular shell seen in *FUSE* spectra of their central stars (Sterling el al. 2002; Sterling & Dinerstein 2003). They detected IR emission from Se and Kr in roughly 50% of their sample PNe from which abundances of up to 10 times solar were derived for these elements. The *FUSE* spectra revealed Ge III absorption in five PNe for which Ge enhancements of 3-10 times solar were deduced, clear evidence that central star AGB progenitors are major sites of *s*-process element production.

As part of our on-going program to detect and identify the weakest lines in PNe at visible wavelengths down to levels significantly below that of the continuum, viz., $< 10^{-5}$ the intensity of Hβ, we have obtained very high signal-to-noise spectra at high spectral resolution of some of the higher surface brightness nebulae. Some fraction of the weaker lines observed are likely to originate from post-Fe peak elements and therefore we have used the automatic line identification routine EMILI (Sharpee et al. 2003), supplemented by recent energy level data for heavier elements, to assist in the search for such lines. Since the publication of PB94, new calculations have been made for spontaneous emission coefficients (Biémont et al. 1995) and collision strengths (Schöning 1997; Schöning & Butler 1998) for fourth and fifth row elemental ion transitions. In this study, we use these newer atomic parameters to compute ionic and overall elemental abundances for Br, Kr, and Xe in order to make comparisons with their abundances in H II regions and the sun, and to derive *s*-process enrichment factors relevant to the study of *s*-process nucleosynthesis in the progenitor stars.

2. Observations and Data Reduction

Our present sample of objects consists of four PNe (IC 2501, IC 4191, NGC 2440, and NGC 7027) which satisfy the most important criteria for the detection of weak emission

lines in having (a) high surface brightnesses, (b) low expansion velocities, and (c) except for NGC 7027, relatively small internal dust extinction. The latter two criteria produce sharper lines and higher peak intensities relative to the continuum.

We obtained spectra of the PNe IC 2501, IC 4191, and NGC 2440 during two observing runs of two nights each in early 2003 using the Las Campanas Observatory (LCO) Baade 6.5m telescope with the MIKE echelle spectrograph. Similar instrumentation setups were used during the two runs. MIKE is a dual-beam spectrograph which simultaneously measures separate red and blue spectra, giving useful data over the continuous wavelength ranges 3280–4700 Å and 4590–7580 Å at resolutions ($\lambda/\Delta\lambda$) of 28,000 and 22,000, respectively, for the 1 arcsec slit width we used.

A series of long and short exposures were taken of each nebula on one or more nights, typically adding up to a period of 2-3 hours at a time spent observing each object. Because MIKE is used without an image rotator at a Nasmyth focus, the orientation of the slit with respect to each nebula rotated by a large amount during these series of exposures. The central star was placed along a line perpendicular to the spectrograph slit so that the slit center was roughly midway between the central star and outer edges of the nebula, and then the telescope was guided to keep the star in that same position as seen on the acquisition/guide TV. The result was that during the course of the observations the slit swept out an arc about the central star, so that the final spectrum integrates over an area of the nebula that is much larger than the 1×5 arcsec slit. The total integration times in the combined long exposures were 630 min for IC 2501, 450 min for IC 4191, and 330 min for NGC 2440. A journal of the observations is given in Table 1, and includes the approximate position of the center of the slit with respect to each of the central stars at the start of the series of exposures.

The optics of the MIKE spectrograph introduce strong distortion into the image formed on the detector, so the projected emission lines have significantly different tilts as a function of their position upon it. When extracting spectra of objects such as these PNe which fill the slit, the tilts introduce unacceptable smearing in the wavelength direction (typically 3 pixels over the 40 pixel slit length) unless they are corrected for during the extraction of the one-dimensional spectra from the two-dimensional echelle image. We wrote our own set of auxiliary FORTRAN programs to calibrate the tilts and perform the proper extraction. This procedure was tested on the emission lines in the comparison lamp spectrum. Compared to the emission line from a single pixel at the slit center, lines summed over the full slit length came out at the same pixel location in the dispersion direction and were broadened by 2 percent on average. We are thus confident that the effects of these tilts are negligible in the extracted PNe spectra. These tilt-corrected spectra were then fed into the same suite of IRAF-based reduction programs used with the NGC 7027 data as described next.

NGC 7027 was observed on 4 nights in June 2002 with the Mayall 4m Telescope at Kitt Peak National Observatory using the Cassegrain echelle spectrograph. Because we were interested in detecting faint 40–50 km s^{-1} FWHM emission lines over the widest possible wavelength range, rather than in detailed measurements of the line profiles, we used the short UV camera with the 79.1 grooves mm^{-1} echelle grating, cross-dispersing grating 226-1

in first order, and a GG-475 order separating filter. This gave full wavelength coverage from 4600 to 9200 Å at ∼20 km s^{-1} FWHM ($\lambda/\Delta\lambda = 15,000$) resolution with our 2 arcsec slit width, with partial coverage out to ∼9900 Å. On each night we offset to the same position with the slit at PA 145° and centered 0.5 arcsec N and 3.5 arcsec W of the central star, which is the brightest part of the PN shell in Hα emission. Most of the observing time was spent obtaining sequences of 1200s exposures which added up to a total of 680 min of integration time. We also took a number of shorter exposures 30, 60, 120, and 300s in length to measure bright emission lines that were saturated on the longer exposures.

The data for all four PNe were reduced using standard procedures with IRAF-based reduction packages in the same manner that has been described in detail in our discussion of comparable spectra of the PN IC 418 that we obtained previously with the CTIO 4m echelle spectrograph (Sharpee et al. 2004). A correction was made for the presence of Rowland ghosts near strong lines (Baldwin et al. 2000). To correct for flexure and temperature drift effects in the spectrographs, comparison lamp spectra were taken at roughly one hour intervals, and the wavelength calibration for each PN spectrum was made using the comparison lamp taken nearest to it in time. The wavelength fits indicate a 1-σ uncertainty in the wavelength scale that varies over each echelle order, and is of the order 4–6 km s^{-1} for all of our spectra. The spectra were flux calibrated using observations of several spectrophotometric standard stars from Hamuy et al. (1994).

The final extracted flux and wavelength calibrated spectra of all the PNe were used for our line identification and analysis, and are available in FITS format as an electronic supplement to the present article.

3. Emission Line Selection

The line selection procedure is initiated by fitting the continuum of each echelle order of the final spectrum with a smooth function that is pegged to the observed continuum at approximately ten wavelength intervals distributed over each order. We developed an automated procedure that selects what should be reliable continuum points for the fitting by selecting wavelength regions with a paucity of lines. Because bad pixels, artifacts caused by scattered light in the spectrograph due to strong emission lines, and line blends can cause poor fits, the fits were reviewed manually for each order and adjusted as necessary to insure that the continuum representation was valid. An example of the output of the automatic continuum fitting algorithm is shown in Figure 1, where a typical fit prior to manual adjustment is displayed. Once the proper continuum level is established, each order is sampled pixel by pixel to detect emission features, which are defined as regions where the observed flux exceeds the continuum flux by 7σ or more over a wavelength interval equal to or greater than that of the resolution of the spectrograph.

All putative emission features were examined individually by eye and compared with their appearance on the original two-dimensional echelle images to establish their reality. We

have found that all features with fluxes greater than 12σ of that of the continuum, i.e., with S/N> 12, are clearly visible on the echelle images. Since scattered light features usually trail across multiple orders one can generally distinguish such artifacts from real lines by visually examining the images. The most uncertain aspect of the line detection process is distinguishing multiple line blends in real emission features. The expansion velocities of PNe are such that intrinsic line widths do vary by factors of 2-3 with the level of ionization, so it can be difficult to discriminate between one broad line vs. two or more closely spaced narrow lines. Figure 1 gives an example of the features within a selected wavelength region in one of our PNe spectra that have been designated by our software as emission lines.

For detection of the weakest nebular lines, where the distinction between a continuum noise spike and a real feature can be difficult to establish with certainty, we have intercompared the spectra of those PNe that have similar levels of ionization but different radial velocities. Noise spikes do not generally produce features having the width of the instrumental resolution, and instrument artifacts tend to occur on the same place on the detector, which is at different rest wavelengths in the PNe spectra because of their differing radial velocities. Since spectra were obtained on different instruments, (MIKE and the 4-meter KPNO echelle), all significant scattered light ghosts could be detected through comparisons between the PNe spectra obtained with MIKE and the NGC 7027 spectrum. Our final line lists do contain a few weak features having S/N<7 which are present in at least two of the objects.

The telluric nightglow emission spectrum was also sampled by these spectra, as sky subtraction in these extended objects was deemed impractical, particularly in regards to the subtraction adding significant additional noise. However, most nightglow lines were distinguishable on the two-dimensional spectra by their uniform intensity and characteristic shape and size, namely those of the imaging slit. The positions and intensities of prospective nightglow lines were compared to those listed in the telluric feature atlases of Osterbrock et al. (1996) and Hanuschik (2003), and likely matches removed from the nebular list except in those cases where their blending with stronger nebular lines was deemed only a minor contaminant. For lines considered as candidate *s*-process ion transitions, nightglow sources were given additional scrutiny through a comparison with the original spectra of the Hanuschik (2003) atlas, the likely identifications of the atlas lines (Cosby et al. 2006), time-averaged observed intensities of their constituent systems (Cosby & Slanger 2006), and in some cases model spectra of those systems constructed with the molecular simulation code DIATOM (http://www-mpl.sri.com/software/DIATOM/DIATOM.html).

Following the selection of sets of likely nebular lines in each of the PNe, their wavelengths and intensities were determined by single or multiple, in the case of blended features, Gaussian fitting of their profiles and immediate underlying continua. Simple summing was used for the most irregular and ill-defined line profiles with intensity-weighted centroids utilized as wavelengths. Emission lines appearing in multiple orders were then collated and their attributes averaged together. Emission line intensities and wavelengths from short and long duration exposure spectra of each PN were then normalized to a particular fiducial frame.

Line wavelengths were shifted to the nebular rest frame through a comparison with either the Balmer (MIKE PNe) or Paschen (NGC 7027) sequence laboratory wavelengths. Line intensities were de-reddened with the Galactic extinction law of Howarth (1983), utilizing an iterative process involving the magnitude of either the Balmer or Paschen jump, and the Balmer or He II 5-n sequence decrements to establish electron temperatures and c(Hβ) logarithmic extinction at Hβ values. The c(Hβ) values for each PN are in good agreement with those listed in Cahn, Kaler, & Stanghellini (1992). Errors in the final line intensities in all PNe spectra, as determined from the formal errors to the profile and continua fits, are similar to those found for NGC 7027: 41% for I<10^{-5} I(Hβ), 20% for I=10^{-5}–10^{-4} I(Hβ), 11% for I=10^{-4}–10^{-3}, and >6% for I>10^{-3} I(Hβ) on average. This is independent of any errors arising from the reddening correction. For weak lines, where the greatest contributor to uncertainty is the indeterminate level of the true continuum, the formal errors in the fit probably understate the actual uncertainty in the intensity. From random inspection of several lines at the 10^{-5} Hβ intensity level, it is likely that some lines may have uncertainties ranging upwards to 100% in regions where the continuum level is rapidly undulating, complicated by scattered light artifacts from adjacent orders, or affected by strong telluric absorption. Final geocentric offsets and c(Hβ) values are presented in Table 2

Figure 2 presents a histogram showing the fraction of lines in each of the nebulae observed with MIKE for different intensity levels relative to Hβ that we have determined to be real and which also appear in at least one of the other two PNe (the NGC 7027 spectrum is omitted here due to its different wavelength coverage and spectral resolution). The strongest emission lines are all detected in each of the nebulae. Even at intensities down to 10^{-5} Hβ, where S/N$\sim$10 typically, roughly 50% of the weak features identified in the individual PNe also appear in one of the other nebulae, suggesting that they are true nebular lines. The present spectra are among the deepest emission spectra taken of nebulae, revealing some of the weakest lines yet observed. This can be seen in Figure 3, where the cumulative number of lines exceeding a given flux level relative to Hβ is shown for several of the most extensive PNe spectral studies published in the recent literature.

4. Plasma Diagnostics and Abundances

Electron temperatures and densities are presented in Table 3. The IRAF *nebular* package task *temden* (Shaw & Dufour 1995) was used to equate relative intensities of collisionally excited diagnostic lines to densities and temperatures by matching a diagnostic for each from ions of similar ionization energy, and solving for self-consistent values. Each ion was modeled by a five or greater level atom for this purpose, with spontaneous emission coefficients and collision strengths for the five lowest levels drawn primarily from the compilation of Mendoza (1983). Although these are not the default values currently distributed with *nebular*, this atomic data set yielded good agreement in temperature and density among diagnostics in our previous analysis of IC 418, and were utilized in the original *nebular* release. Spontaneous emission coefficients from Froese Fischer & Tachiev (2004) and collision strengths

from Wilson & Bell (2002) were used for N I and Cl II respectively. For the remaining energy levels and for the ions Cl IV and K V, the atomic data used in the most recent release of *nebular* was utilized. The departure of the [K V] density diagnostic from other density diagnostic values, particularly in NGC 2440 and IC 4191, may indicate errors in this atomic data. However, *s*-process elemental abundance derived later using this diagnostic (Kr^{+4}/H^+ and Xe^{+5}/H^+) were completely insensitive to the utilized density. Errors in diagnostic values were determined by selecting the extrema values from computations at all combinations of diagnostic line ratios plus and minus their (1-σ) uncertainties, including an error estimate for the reddening correction. Indeterminate error limits, such as occurred when a ratio value exceeded the asymptotic limit or where the paired diagnostics failed to converge at a particular ratio value, are listed without a value. Balmer (MIKE PNe) and Paschen (NGC 7027) jump temperatures were calculated in the manner described by Zhang et al. (2004), and as reported by them for many PNe, they are lower than those temperatures determined from the collisionally excited lines.

Ionic abundances derived from both collisionally excited and nominal radiative recombination lines are presented in Table 4. The IRAF *nebular* package tasks *ionic* and *abundance* were used to make computations from the collisionally excited lines listed in Table 3 using temperatures and densities derived from the diagnostics with the closest ionization potential to each ion. Where no diagnostics where clearly appropriate, averaged values for temperature and density where used. Uncertainties were computed in the same manner as the diagnostic values, by calculation of the abundance at every combination of temperature, density, and line intensity ratio plus or minus their (1-σ) uncertainties (where available) and selecting the extrema values. Uncertainties were not calculated for abundance computed with averaged diagnostics values. For the recombination lines, effective recombination coefficients were combined with line intensities to make abundance determinations, in the manner described by Sharpee et al. (2004), with temperature and densities again drawn from diagnostics nearest in ionization potential to each ion. For He^+/H^+, the coefficients of Smits (1996) or Benjamin, Skillman, & Smits (1999) were used to determine an average abundance from the λ4923, λ5876, and λ6678 lines, with corrections for collisional excitation (Case A triplets, Case B for singlets) taken from Kingdon & Ferland (1995), while coefficients from Storey & Hummer (1995) were used to calculate an average He^{+2}/H^+ abundances from various He II lines. To determine C^{+2}, N^{+2}, O^{+2}, and Ne^{+2} abundances relative to H^+, recent effective recombination coefficients (Storey 1994; Kisielius et al. 1998; Davey, Storey, & Kisielius 2000; Kisielius & Storey 2002) for the strongest observable multiplets were used to calculate abundances. As seen in Table 4, O^{+2}/H^+ and Ne^{+2}/H^+ abundances deduced from the collisionally excited lines are systematically lower than those derived from radiative recombination lines, as is generally the case in PNe (Liu 2004; Robertson-Tessi & Garnett 2005).

5. Emission Line Identification

The emission line identification code EMILI (Sharpee et al. 2003) was used to make the majority of emission line identifications. EMILI creates models of the ionization-energy dependent velocity field and ionization level of a PN or H II region from user-supplied empirical data. These models are used by EMILI to select from a large atomic transition database all transitions within five times an observed line's wavelength measurement error, and to compute relative intensities for emission lines corresponding to those transitions. Those transitions predicted to produce emission line intensities within 3 orders of magnitude of the highest value among all transitions initially selected are then subjected to a test for the presence of lines from the same LS-coupled multiplets (but not all lines from the same upper level) at expected wavelengths and relative intensities. Potential identifications are then assigned a numeric likelihood parameter based on their wavelength agreement with the observed line, strength of the predicted emission line, and results of the multiplet check, and are ranked and presented.

Many emission lines from Z>30 elemental ions were observed in NGC 7027 by PB94. To place these lines on an equal footing for identification purposes with those arising from more abundant lighter elements, EMILI used the Atomic Line List v2.05 of P. van Hoof[1] as its reference database, which extends to Z=36 (Kr). The latest experimental determinations available in the literature for ground electron configuration energy levels of Z>36 ions were then added to this database. Transition wavelengths for the mostly optically forbidden transitions among these levels were constructed by differencing the level energies. Sources for all Z>30 ion energy levels and associated atomic data used in subsequent analysis are provided in Table 5. All ions with certain or probable line identifications in NGC 7027, as rated by PB94, most of those with more tenuous identifications, and a handful of other ions they suggested to be worthy of future consideration at a higher spectral resolution, were incorporated into the database. However, ions with level uncertainties perceived or explicitly stated to be greater than 1.0 cm^{-1} in their source literature were excluded.

EMILI was run against each nebula's set of observed emission line wavelengths and intensities. Electron temperature and density values were provided to EMILI by the results of standard plasma diagnostics, derived from strong collisionally-excited lines with certain identifications. Construction of the empirical kinetic and ionization models were also drawn from those same lines. The EMILI reference elemental abundances were set to the solar values of Lodders (2003). EMILI was also run against the IC 418 line list of Sharpee et al. (2003), to determine if some of its remaining unidentified lines could be identified with an expanded set of transitions, and to also act as a foil for the mostly higher excitation PNe considered in the present sample. The line identification lists produced by EMILI were then visually inspected, and the EMILI-preferred assignments were compared to identifications in the literature for those same lines in PNe and H II region spectra of similar depth, spectral

[1]http://www.pa.uky.edu/p̃eter/newpage/

resolution, and level of ionization. The entries in our final line list are in many cases taken from among the highest-ranked EMILI suggested identifications.

A segment of a final line list is given in Table 6; the full line list is available in the electronic version of this manuscript. This table lists all observed lines with their characteristics, viz., observed wavelength in the nebula rest frame, identifications, full widths at half maxima, S/N, observed and reddening corrected intensities relative to Hβ, and their most likely identifications. Lines with uncertain identifications are denoted by a ":", likely blends with a "bl" or "ns" if blended with a telluric emission feature, and uncertain features are marked with a "?". Only the perceived strongest component of a blend is listed in the table. Lines without obvious identifications are listed here without an identification.

6. Z$>$ 30 Line Identifications

PB94 detected 25 emission lines from several Z>30 ions in their optical spectra of NGC 7027, including Se, Br, Kr, Rb, Sr, and Y from the fourth row of the periodic table, Xe and Ba from the fifth row, and Pb from the sixth. Eighteen of these detections were considered "certain" or "probable", and 7 considered "possible". Lines from 13 additional Z>30 ions were also either tentatively identified or proposed as future targets for spectra with greater spectral resolution and better S/N.

Given the depth and high-resolution of the spectra considered here, confirmation of the PB94 identifications in multiple PNe was sought, as were additional lines belonging to other Z>30 ions. The use of EMILI allows prospective Z>30 transitions and weaker transitions of more abundant lighter elements to be treated equally for purposes of emission line identification. Collision strength and spontaneous emission coefficient calculations for these transitions allow accurate predictions to be made of the relative intensities of lines arising from the same ion, allowing identifications of their lines to be made with more confidence.

The line lists for the present PNe sample and IC 418 (Sharpee et al. 2003) were searched for the strongest expected Z>30 ion transitions within their observed bandpasses. These primarily were the $^3P_{1,2}$–$^1D_2$ nebular transitions of ions with $4p^{2,4}$ and $5p^{2,4}$ valance electrons, the $^4S^o_{3/2}$–$^2D^o_{3/2,5/2}$ nebular transitions of ions with $4p^3$ and $5p^3$ valence electrons, and the $^2P^o_{1/2,3/2}$–$^2P^o_{1/2,3/2}$ fine-structure transitions for 4p, $4p^5$, 5p, $5p^5$, and 6p valance electron ions. Fine structure ^3P–^3P transitions, when accessible in the visible, were also included. For the cases of Kr IV, Xe IV, and Br IV, auroral $^2D^o_{3/2,5/2}$–$^2P^o_{1/2,3/2}$ and trans-auroral $^4S^o_{3/2}$–$^2P^o_{1/2,3/2}$ transitions were also considered. The permitted resonance lines of Ba II and Sr II were also searched for. Initially, all wavelength coincidences of 1Å or less between an observed line and a transition wavelength were considered possible Z>30 lines, regardless of the identifications recommended by EMILI for those lines.

Tables 7– 10 present excerpts from the EMILI output for observed lines believed to represent the best cases for a Z>30 transition as the actual identification for an observed line in

at least one of the PNe in which that line appeared. For each observed line in each PN, the identifications of highest rank, as specified by the "Identification Index" or IDI, the EMILI figure-of-merit for quality of an identification (5 or less is considered a quality identification), and their multiplet search statistics (numbers expected/observed, hereafter multiplet statistics) are included. The IDI value is followed by a letter A→D if among the top four highest ranked transitions, with "A" being the highest. Additional identifications drawn from the literature and from the terrestrial nightglow (prefaced with "SKY") are also included. Identifications that did not yield predicted line intensities within three orders of magnitude of the strongest value among all identifications, or were outside the 5-σ search radius, do not have a calculated IDI value. The IDI value/rank is sometimes followed by a symbol, an asterisk indicating the most likely single identification, "bl" indicating components of a likely blend, and ":" indicating indeterminate alternate identifications. The reddening corrected intensity of the feature attributable to the putative s-process identification, if corrected for any blending as described in succeeding sections (due to other identifications denoted with a "bl"), is presented in italics below its originally observed value. The limiting intensity, determined from the local minimum flux of line detection considered certain (S/N=7), or from imposition of artifical lines of S/N=7 at that wavelength, is presented in brackets for the case of s-process transitions without corresponding observed features. An "OUT" label indicates features residing outside the observed bandpass of a spectrum. Finally, features of dubious reality are denoted by a "?" following the observed wavelength.

Figure 4 depicts continuum-subtracted spectra, with wavelengths shifted to the nebular rest frame, in the vicinity of those Kr, Xe, and Br lines for which a positive identification was made in at least one PN, and which were potentially observable in all four PNe of the present sample and in IC 418. Comments on identifications pertaining to individual Z>30 elemental ion lines follow.

6.1. Kr Line Identifications

PB94 noted that [Kr III] $4p^4\ ^3P_2$–$4p^4\ ^1D_2$ λ6826.70 has long been observed in various novae and PNe, but has seldom been identified as such. They identified [Kr III] as a strong line in NGC 7027, blended with weak C I (V21) λ6828.12 and He I 3s ^{3}S–16p $^3P^o$ λ6827.88 lines.

As seen in Table 7 and Figure 5, the higher resolution of our present PNe spectra cleanly separates both the He I and C I line from the putative [Kr III] line, except for NGC 7027, where He I contributes minimally to its red shoulder. However, Figure 5 shows that the R branch head of the telluric nightglow OH Meinel 7-3 band is a serious contaminant in this region. In NGC 7027, a broad O VI λ1032 Raman scattering line at λ6829.16, seen previously in NGC 7027 by Zhang et al. (2005), is also observed. The OH contribution was represented by a model of the band normalized in intensity to the uncontaminated $R_1(1.5)$ line at λ6834.01. The He I 3s ^{3}S–15p $^3P^o$ λ6855.91 line profile was shifted and scaled by a factor of 0.83 to represent He I λ6827.88 (Smits et al. 1991; Case B, for the most appropriate

grid point: T_e=10^4K, n_e=10^4 cm^{-3}). The profile of the companion O VI Raman scattering line observed at λ7088, scaled upwards by a factor of four to yield the best fit with the red wing of the putative [Kr IV] feature, represented the λ6829.16 line. These line profiles and the telluric model were subtracted from the continuum normalized spectra to yield the residual features shown in Figure 5.

For all PNe except NGC 2440, where the observed line appears to be entirely comprised of the OH line, there appears to be a substantial residual feature that is coincident, but except for IC 4191, slightly to the red of the predicted wavelength for [Kr III] λ6826.70. The EMILI results for the corresponding observed lines suggest that besides the C I and He I transitions mentioned earlier, the [Fe IV] λ6826.50 feature is probably the only other sensible alternative identification. However, given the absence of other multiplet members that should be observed with this line and the relative observed strengths of the likely strongest [Fe IV] lines (Rodríguez 2003), this is not a likely identification except perhaps for IC 4191. Unfortunately, the companion [Kr III] $^3P_1$–$^1D_2$ line at λ9902.3, predicted to be ∼18 times weaker by Biémont & Hansen (1986b), is only potentially observable in NGC 7027, where a line listed at λ9903.55 is much too strong and most likely associated with C II 4f $^2F^o$–5g ^{2}G λ9903.67. Nevertheless, we conclude that the [Kr III] λ6826.70 identification is relatively certain in IC 418, IC 2501 and NGC 7027, uncertain in IC 4191, and that line is not observed in NGC 2440.

Examination of Table 7 shows that both transitions of the [Kr IV] $^4S^o$-$^2D^o$ nebular multiplet $\lambda\lambda$5346.02,5867.74 are clearly identified in every spectrum, appearing as the primary EMILI ranked identifications. For λ5346.02, the [Fe II] λ5347.65 identification is clearly too far away and the S II (V38) λ5345.71 dielectronic transition is unlikely given the absence of other multiplet members. The Al II λ5867.8 identification for λ5867.74, given by Baldwin et al. (2000) and Sharpee et al. (2003), is clearly superseded. With a theoretical intensity ratio I(λ5346.02)/I(5867.74) of 0.65 (Schöning 1997), assuming electron densities well below the critical density values of ∼18–1.3×10^7 cm^{-3} for the $^2D^o_{3/2}$ and $^2D^o_{5/2}$ levels respectively, as justified from the values in Table 5, the observed λ5346.02 intensity appears to be somewhat too high for IC 4191 and IC 418. This suggests the possible blending of [Kr III] λ5346.02 with another transition, perhaps C III (V13.01) λ5345.85, although poor multiplet statistics and the weakness of the strongest C III lines in IC 418 cast doubt on this possibility for that PN. However, the other three PNe have ratios of 0.76 (NGC 2440), 0.72 (IC 2501), and 0.73 (NGC 7027), which are slightly higher but consistent with the expected value within the combined measurement errors of the line intensities.

The auroral [Kr IV] $^2D^o_{3/2,5/2}$-$^2P^o_{3/2}$ $\lambda\lambda$6107.8,6798.4 identifications are less straightforward, except for NGC 7027 where both are considered certain according to both PB94 and the present EMILI results. In NGC 2440, the observed line corresponding to the λ6798.4 transition, which should be 2.5 times weaker than λ6107.8 (Biémont & Hansen 1986b), is actually stronger, while in IC 2501 the stronger λ6107.8 line is not present at all. As suggested by both PB94 and the EMILI results, C II (V14) λ6798.10 may be responsible for either the total intensity in IC 2501 or excess intensity in NGC 2440. While PB94 note that C II

(V14) is of dielectronic recombination origin and its multiplet components should not have relative intensities expected due to LS-coupling rules, an examination of the intensities of all lines from this multiplet appearing in each PN suggests that the intensities do appear to roughly follow those rules with the exception of what would be the strongest line at λ6783.91. Therefore, as an approximation, a LS-coupled relative strength of λ6798.10 to λ6791.47 of 0.16, instead of the one-to-one ratio with λ6812.28 used by PB94, was utilized to correct the putative [Kr IV] λ6798.4 feature in both NGC 2440 and NGC 7027, as λ6812.28 appears itself appears in only one of the PNe spectra (it would be the weakest feature in the multiplet if LS-coupling rules held). Subsequent abundance analysis also suggests that the [Kr IV] λ6107.8 line itself may be too strong relative to its nebular counterparts in NGC 2440 and IC 4191, admitting [Fe II] λ6107.28 as an alternate identification that appears more likely in the latter PN. In summary, both auroral transition can only be identified comfortably in NGC 7027.

The third magnetic dipole transition of the [Kr IV] auroral multiplet $^2D^o_{3/2}$–$^2P^o_{1/2}$ λ7131.3 is not definitively detected in any spectrum including NGC 7027. However, in the NGC 7027 spectrum, a feature is observed at λ7131.65 with intensity 7.7×10^{-5} I(Hβ), comparable to λ6107.8. It originally was assumed to be an under-corrected Rowland ghost arising from the nearby saturated [Ar III] $^3P_2$–$^1D_2$ λ7135.80 line, but might instead be associated with λ7131.3. The electric quadrupole line [Kr IV] $^2D^o_{5/2}$–$^2P^o_{1/2}$ λ8091.0 is forty times weaker and therefore undetectable.

PB94 claim a detection of [Kr V] $^3P_1$–$^1D_2$ λ6256.06 as a blend with C II (V10.03) λ6257.18 at their instrumental resolution. In our spectra, as is shown in Figure 5, C II λ6257.18 is resolvable from the putative [Kr V] feature in all spectra except NGC 7027, where it slightly contributes to its red wing. However, in IC 2501 and NGC 7027, as also noted by Zhang et al. (2005), another C II line, dielectronic C II (V38.03) λ6256.52, is believed to be a significant contaminant in some PNe based upon the strength of the nearby λ6250.76 line from the same multiplet and upon favorable EMILI assessments. The profiles of both C II lines were approximated and subtracted from all the PNe spectra in Figure 5, where the C II (V10.03) λ6259.56 line profile scaled downward by a factor of 0.56 represents λ6257.18, and the C II λ6250.76 profile, also scaled downward by a factor of 0.56 according to LS-coupling statistics, represents λ6256.52. The contribution of the interloping telluric OH 9-3 band was accounted for through subtraction of a model of the band normalized in intensity to the nearby $Q_1(2.5)$ λ6265.21 line.

The resulting residual plots show a distinct line just to the red of the predicted wavelength of [Kr V] λ6256.06 in NGC 2440, IC 2501, and NGC 7027, that we believe can be definitely identified as such in all three PNe. For IC 4191, the residual flux, 3.0×10^{-6} I(Hβ), is probably too low to be an actual line, and the entirety of the original profile is ascribed here to C II (V38.03) λ6256.52, particularly since both the original line and λ6250.76 share the same broad profile in the spectrum. In IC 418, the putative [Kr V] profile is completely removed by the combination of the nightglow and C II (V38.03) λ6256.52 model profiles, as is appropriate given the nebula's low excitation.

The other nebular line, [Kr V] $^3P_2$–$^1D_2$ λ8243.39, accessible only in the bandpasses of the NGC 7027 and IC 418 spectra, sits amidst the head of the Paschen series, rendering it difficult to disentangle at the resolution of our NGC 7027 spectrum. In the IC 418 spectrum, a comparable observed line is indistinguishable from other nearby lines in the Paschen series and is clearly identifiable as H I 3–43 λ8243.39, with the Kr V identification unlikely due to the PN's low ionization level. Returning to NGC 7027, PB94 identified this transition at λ8242.7 as a blend with N I (V2) λ8242.39 and O III 5g G $^2[9/2]^o$–6h H $^2[11/2]$ λ8244.10, compromised by telluric absorption. In our NGC 7027 spectrum, [Kr V] λ8243.39 is tentatively identified as the blue peak at λ8244.33 of a resolved two-line blend with H I 3–42 λ8245.64, and which appears significantly affected by telluric absorption. The alternate identification for the line, N I λ8242.39, is clearly resolved here as a separate feature. Because this observed line has a measured intensity ratio with λ6256.06 roughly comparable to what would be expected if both lines were due to [Kr V], I(λ6256.06)/I(λ8243.39)=1.1 (Biémont & Hansen 1986a), it is believed that O III λ8244.10 contributes only a minor amount to the line, although the presence of the telluric absorption complicates matters. To summarize, both [Kr V] lines appear to be present with about the expected intensity ratio in the spectrum of NGC 7027, but both are absent in the spectrum of IC 418. For the cases of IC 2501 and NGC 2440, [Kr V] λ6256.06 is probably present.

The spectra were also examined for evidence of other auroral and trans-auroral transitions of Kr ions. Only the auroral line [Kr V] $^1D_2$–$^1S_0$ λ5131.78 satisfied the initial $\pm$1Å screening criterion and also appeared in the EMILI output as a possible identification for an observed line at $\sim$5131.0Å in all PNe. The case for this identification is lessened by the expected weakness of this line compared to other [Kr V] lines that were not definitively identified, and particularly because of its high observed intensity of 1.3×10^{-3} I(Hβ) relative to the $\sim 1 \times 10^{-4}$ I(Hβ) for $\lambda\lambda$6256.06,8243.39 in NGC 7027, the nebula that might be expected to exhibit the best evidence for this line given the strength of the other confirmed Kr lines. Instead either O I 3p ^3P–8d $^3D^o$ λ5131.25, which was the highest ranked line in all but one nebula (IC 418) and that has a strength comparable to other members of the same sequence, or C III 5g ^3G–7h $^3H^o$ λ5130.83 appear the more likely identifications.

6.2. Xe Line Identifications

A number of Xe ion transition identifications are also considered probable in our spectra. The EMILI statistics for Xe identifications are affected by the low solar Xe abundance, which is an order of magnitude lower than Kr (Lodders 2003). This contributes to low predicted relative emission line intensities and consequently higher or absent IDI values for its identifications as compared to those computed for weak transitions from more abundant elements. As such, every appearance of a Xe ion transition as a candidate identification for an observed line in an EMILI list, regardless of its IDI value, was given serious consideration as it signaled that alternative identifications from more abundant elements did not predominate despite the advantage arising from greater abundances. Table 8 lists the EMILI statistics

for lines judged most likely to correspond to Xe ion transitions, while Figure 4 depicts the regions around the most likely observed transitions.

The identification of [Xe III] $^3P_2$–$^1D_2$ λ5846.77 in NGC 7027, was given by PB94 to an excess intensity in the He II 5–31 λ5846.66 line. This excess was searched for in the present PNe sample through the subtraction of the He II λ5837.06 profiles, shifted to the λ5846.66 line position and scaled assuming I(λ5837.06)/I(λ5846.66)=0.92 (Storey and Hummer 1995; Case B, for the most appropriate grid point: T_e=10^4K, n_e=10^4 cm^{-3}) as is shown in Figure 6. The intensity of He II λ5837.06 was not corrected for the presence of C III 7h $^3H^o$–18i ^3I λ5836.70 because the line used for this correction by PB94, C III 7i ^3I–18k $^3K^o$ λ5841.2, was either not present or was an identification of low rank (IDI=6, ranked 5th) for a corresponding line in NGC 7027. As seen in Figure 6, distinct residual profiles are present after subtraction of He II λ5846.66 for both NGC 7027 and IC 418 (the latter having negligible He II), and at the correct wavelength for [Xe III] λ5846.77. A bizarrely shaped profile is seen for IC 2501, and no profiles are seen for either NGC 2440 or IC 4191 after subtraction. While the corresponding observed lines are probably He II λ5846.66 in the latter two PNe, IC 2501 has very weak He II lines, suggesting that the residual profile is attributable to something else, tentatively [Xe III] λ5846.77. The [Xe III] λ5846.77 identification, while not appearing in the EMILI lists for NGC 7027 or IC 2501, is considered a better choice than the other top ranked identification, [Fe II] λ5847.32, which has poorer wavelength agreement and multiplet statistics in all cases. While the [Xe III] $^3P_1$–$^1D_2$ transition at 1.37μ is unavailable for confirmation, we believe that the [Xe III] λ5846.77 is definitely present in NGC 7027 and IC 418, but is only tentatively identified in IC 2501.

The reality of the observed features potentially corresponding to the [Xe IV] $^4S^o_{5/2,3/2}$–$^2D^o_{3/2}$ $\lambda\lambda$5709.2,7535.4 transitions is marginal except in NGC 7027. However, their identifications as the Xe lines, should they be actual emission lines, is more certain. For λ5709.2, the widely observed N II (V3) λ5710.77 line is detected as a separate line in all of the spectra. Alternative identifications such as [Fe I] a$5D_3$–a$5P_1$ λ5708.97 either have too many missing multiplet members, except for IC 2501 where the ratio of potentially observed to total number of multiplet lines expected is marginally better, or as in the case of the Fe II] λ5709.04 intercombination line, unlikely given that permitted Fe II lines were not anywhere definitively identified. For λ7535.2, the reality of the observed lines is less uncertain, including IC 418 where a previously unreported line has been uncovered by more thorough examination of its spectra. The Fe II] (V87) λ7534.82 identification proposed by Hyung et al. (2001) is unlikely for the same reasons as Fe II] λ5709.04 for [Xe IV] λ5709.2. The N II 5f G $^2[7/2]_4$–10d $^1F^o_3$ λ7535.10 identification, selected by Esteban et al. (2004) and Peimbert et al. (2004), also appears unlikely given the relative strengths of other known permitted N II lines in the spectra. It should be noted that the EMILI statistics for the λ7535.10 identifications in the MIKE PNe sample would probably have been better if the line did not appear near the end of the last spectral order where the wavelength calibration is the poorest. Assuming an electric density well below the critical regime ($\sim 10^7$ cm^{-3}), the expected intensity ratio is I(λ5709.2)/I(λ7535.4)=0.64 (Schöning & Butler 1998). The observed range of values that we observe, 0.33–1.19, suggests measurement errors on par with the average values for such

weak lines. The strongest examples in NGC 7027 do yield the best agreeing ratio (0.82). As such, we conclude that both [Xe IV] lines may be present in all PNe spectra with varying degrees of certainty.

One of the stated goals for future spectroscopy of NGC 7027 and other PNe given by PB94 was the detection of [Xe V] transitions, none of which they detected with any certainty. In the present spectra, no observed line passed the ±1Å initial selection criterion for the $^3P_{1,2}$–$^1D_2$ $\lambda\lambda$5228.8,6998.7 lines, nor did these transitions appear as possible EMILI IDs for any observed line. This is despite the improved sensitivity and resolution which should have enhanced the chances of detecting λ5228.8, and which should have easily separated λ6998.7 from O I (V21) λ7002.10, the contaminant noted by PB94. Nevertheless, the detection of these lines in our spectra would remain problematic since for λ5228.8 extensive flaring from [O III] λ5006.84 in an adjacent order leads to numerous ghosts in its vicinity, while for λ6998.7 telluric absorption in the tail end of the Fraunhofer A band complicates its observability.

EMILI did suggest that the fine-structure transition [Xe V] $^3P_0$–$^3P_2$ λ7076.8 as a possible identification for observed lines in two PNe, IC 4191 and NGC 7027, PNe with appropriate excitation levels for the appearance of a line of this ion. This is the primary EMILI identification in IC 4191. A third occurrence of the corresponding observed line in NGC 2440 is clearly associated with a nightglow line from the O_2 $b\,^1\Sigma_g^+$–$X\,^3\Sigma_g^-$ 3-2 band upon comparison with a simulation of that band. The competing identification C I (V26.01) λ7076.48 has poor multiplet statistics, while [Fe III] λ7078.10 and [Ni II] λ7078.04 are feasible, but have poor wavelength agreement. The Ca I identifications are also unlikely given that they arise from energy levels of large energy, where lines that would follow from cascades from these levels are not observed. Two remaining obstacles to an identification with [Xe V] λ7076.8 are the lack of the nebular ^3P–^1D lines and the low branching ratio for this electric quadrupole transition ($\sim$0.008 with respect to $^3P_1$–$^3P_2$ at 2.07μ). Nevertheless, despite this transition's expected weakness, the lack of viable alternate identifications suggests the corresponding observed line may be at least tentatively identified in NGC 7027, and probably identified in IC 4191, and both occurrences yield reasonable abundance values in subsequent analysis.

The fine structure transition [Xe VI] $^2P^o_{1/2}$–$^2P^o_{3/2}$ λ6408.9 was identified with certainty in NGC 7027 by PB94. In the present NGC 7027 spectrum, λ6408.9 is probably associated with a weak but clearly separable observed line on the red wing of He II 5–15 λ6406.38. The alternate primary EMILI identification of [Fe III] λ6408.50 was not considered likely, as an inspection of the NGC 7027 spectrum for other lines from all low energy [Fe III] multiplets did not show a significant number of matches to warrant strong consideration as a likely identification. [Fe III] λ6408.50 also has a comparatively high excitation energy (6.25 eV). A C IV 9–17 λ6408.70 identification is similarly downgraded by its high excitation. The reality of corresponding observed lines in NGC 2440 and IC 4191 is questionable, although for lack of suitable alternate identifications, uncertain identifications of [Xe VI] λ6408.90 are retained for both.

As with Kr, an inspection for auroral and trans-auroral transitions of various Xe ions was

also undertaken. There were coincidences within ±1Å between the [Xe III] $^3P_1$–$^1S_0$ λ3799.96, [Xe III] $^1D_2$–$^1S_0$ λ5260.53, [Xe IV] $^4S^o_{3/2}$–$^2P^o_{1/2}$ λ3565.8, [Xe IV] $^2D^o_{3/2}$–$^2P^o_{3/2}$ λ4466.5, [Xe IV] $^2D^o_{5/2}$–$^2P^o_{3/2}$ λ5511.5, [Xe IV] $^2D^o_{3/2}$–$^2P^o_{1/2}$ λ6768.9, and [Xe V] $^1D^2$–$^1S_0$ λ6225.3 lines. However, except for two instances, the identifications did not appear in the EMILI list for those particular lines, and most had more reasonable and higher ranked, identifications: C II (V30) λ5259.66,.76 for example instead of the auroral [Xe IV] λ5260.53 line. In many cases the line only appeared in one of the PNe spectra analyzed here, and could be rejected due to the strength or absence of the nebular transitions from the same ions.

6.3. Br Line Identifications

In PB94 two transitions of Br were identified: [Br III] $^4S^o_{3/2}$–$^2D^o_{5/2}$ λ6131.0 with certainty, and [Br IV]$^2D^o_{3/2}$–$^2P^o_{3/2}$ λ7385.1 as possible. A second nebular transition, [Br III] $^4S^o_{3/2}$–$^2D^o_{5/2}$ λ6556.4, was lost in a blend amidst the [N II] λ6548.04+Hα+[N II] λ6583.46 complex.

The source for the Br III levels in the Atomic Line List v2.05 is Moore (1958), while the source used by PB94 is stated to be the experimental levels listed in Table IV of Biémont & Hansen (1986a) from unpublished work of Y.N. Joshi and Th.A.M. van Kleef, and provided by private communication with van Kleef. However, a comparison of the Ritz-determined wavelengths from both sets of levels with those listed by PB94 shows that the Joshi and van Kleef $^2D^o$ term energy levels were used for the nebular transition wavelengths, while the Moore (1958) levels were used for auroral transition wavelengths. The substantial difference in the $^2D^o_{3/2}$ level energy, 15042 cm^{-1} for Moore (1958) and 15248 cm^{-1} for Joshi and van Kleef, leads to a difference in the $^4S^o_{3/2}$–$^2D^o_{3/2}$ transition air wavelength of 6646.3 Å versus 6556.4 Å, respectively, with a lesser difference for the other transition, 6132.9 Å versus 6131.0Å. Since the Moore (1958) levels used by the Atomic Line List v2.05 and therefore by EMILI have stated uncertainties of 0.63 cm^{-1}, while those for Joshi and van Kleef in Table IV of Biémont & Hansen (1986a) are listed to a precision 1 cm^{-1}, nearly the same level of uncertainty, it is difficult to know which levels are more accurate. Therefore, EMILI was run using both sets of energy levels, and the $^4S^o$–$^2D^o$ lines were searched for at both sets of resultant wavelengths.

For the transitions wavelengths generated from the Moore (1958) energy levels, λ6132.9 and 6646.3, no observed line was detected in any spectrum meeting the initial ±1Å selection criterion. However, for the $^4S^o_{3/2}$–$^2D^o_{5/2}$ transition wavelength generated from those energy levels used by PB94, λ6131.0, there do appear to be observed lines in 4 of the 5 PNe spectra near the λ6130.4 line that PB94 identified with [Br III]. As seen in Table 9, while [Br III] λ6131.0 is the highest ranked EMILI identification in only one PN.

However, other identifications for the putative [Br III] λ6131.0 line are not compelling. PB94 cite their observed line as being a blend with C III 7h $^{1,3}H^o$–16g $^{1,3}G$ λ6130.30, which is the highest EMILI-ranked transition in each spectrum in which the putative Br III line is observed, except for IC 2501. However, the companion line C III 7h $^{1,3}H^o$–16i $^{1,3}I$ λ6126.30,

claimed by PB94 to have an equal intensity to λ6130.30, is not present in either the IC 4191 and IC 418 spectra. Well-known lower excitation C III lines are of negligible intensity in IC 418, while in IC 2501 C III λ6126.30 has poor wavelength agreement with its corresponding observed line, and is not the primary EMILI identification for that line. Only in NGC 7027 is C III λ6126.30 a primary ID, suggesting that only in its spectrum is the equally intense C III λ6130.30 likely to be present and accountable for at least a portion of the putative [Br III] λ6131.0 line. As such for NGC 7027, the λ6126.30 line intensity is subtracted from the observed line at 6130.32Å, while in the remaining spectra the corresponding observed lines are ascribed wholly to [Br III] λ6131.0. Possible contamination due to flaring from an adjacent order in the NGC 7027 spectrum was not accounted for. The [Ni VI] λ6130.40 identification, the second ranked identification in many of the spectra, is of high excitation (8.3 eV upper level), too high an ionization for IC 418, and appears only to be ranked highly due to a favorable coincidence in wavelength.

Spectroscopic confirmation for this identification is sought in the possible presence of the [Br III] $^4S^o_{3/2}$–$^2D^o_{3/2}$ λ6556.4 transition, in the PNe spectra at expected intensities similar to that of λ6131.0. As mentioned, detection of this line is difficult given its proximity to the saturated Hα line and its associated ghosts in its immediate proximity. Nevertheless, inspection of the line lists and spectra (Figure 4) does show distinct co-aligned features in the IC 2501, IC 4191, and NGC 7027 spectra near this wavelength. While initially assumed to be ghosts, the fact that these features can be found in spectra from two different instruments and appear invariant to the Hα intensity, suggest they may be unrelated to Hα. That real lines can be observed between [N II] λ6548 and Hα is demonstrated by the presence of the strong telluric OH $P_1(3.5)$ 6-1 λ6553.62 line just to the blue of the suspected [Br III] feature. EMILI lists the [Br III] λ6556.4 identification among possible choices in all PNe in which the line appears, with the λ6131.0 identification satisfying the multiplet search in IC 2501 and IC 4191. Alternate EMILI-favored identifications for these features correspond to O II, and N II permitted and core-excited transitions between levels of primary quantum number 4–6, and are doubtful as they are of comparatively high excitation with respect to better-known 3–3 or 3–4 transitions in these PNe that have equal or lesser intensities. They appear here only due to their wavelength agreement with the observed lines. The highest ranked Fe II λ6555.94 is discounted once again by the lack of other permitted Fe transitions in any spectra.

The observed intensity ratios of the two putative [Br III] lines, I(λ6131.0)/I(λ6556.4), ranging from 0.18–0.45, do conflict with theoretical expectation as follows. While specific collision strengths are unavailable at present for the Br III states, the ratio of the strengths relevant to these transitions should still be roughly proportional to their respective upper level statistical weights (Péquignot & Baluteau 1994; Osterbrock & Ferland 2006), weighted by a Boltzman factor respecting the difference in level energies, and non-negligible fine-structure emission between the $^2D^o$ levels, at sub-critical electron densities. Employing the IRAF *nebular* package task *ionic* to solve for the relative populations of the $^2D^o$ levels at temperature derived from the diagnostic thought to be the most appropriate, from [Ar III], and using appropriate Kr IV collision strengths as a proxy, scaled as discussed in Section 7,

the I(λ6131.0)/I(λ6556.4) ratio is expected to be 0.72–0.83. This is close to the 0.67 value expected from the ratio of the collision strengths alone, and two to three times larger than the ratio observed in the spectra. At these levels the [Br III] λ6131 line should have been observable in NGC 2440, as the predicted intensity exceeds the likely detection limit for features in its vicinity. Therefore, we consider [Br III] to have been only tentatively detected in NGC 2440. However, at least one [Br III] line does appear to be present in the remaining four PNe. They all have lines detected at the same wavelengths, although shifted 20–30 km s^{-1} to the blue of the wavelengths we have adopted for the [Br III] lines, at approximately the same relative intensities, and lack satisfying alternate identifications. The ratio of observed intensities (or in the case of IC 418 the upper limit), while not exact, are within a factor of 2–3 of those expected.

The identifications of the nebular [Br III] lines suggests that the level energies of Moore (1958) for at least the $^2D^o$ term levels may be in error. PB94 also identified an observed line at 7384.3Å as possibly auroral $^2D^o_{3/2}$–$^2P^o_{3/2}$ λ7385.2, but no such line appears in any of the PNe spectra examined here. However, since PB94 appears to have used $^2P^o$–$^2D^o$ transition wavelengths derived from the Moore (1958) energy levels, this might not be a surprise, although no lines in any PN were discovered at the corresponding wavelength for the $^2D^o_{3/2}$–$^2P^o_{3/2}$ transition (7483.1 Å) computed from the levels listed by Biémont & Hansen (1986a) either.

The nebular [Br IV] $^3P_1$–$^1D^2$ λ7368.0 line was detected by PB94 at 7366.0Å, affected by telluric absorption, and blended with C IV 10–21 λ7363.9 and O III 4s $^3P^o_1$–4p $^3P_1$ λ7365.35. In our NGC 7027 spectrum, a line appearing at 7367.62Å as a small protrusion above the local continuum level interpolated between telluric absorption features in both spectral orders covering that wavelength, is tentatively identified as [Br IV] λ7368.0. The alternate candidates listed by PB94, dielectronic C II 3p′ $^2D_{5/2}$–3d′ $^2P^o_{3/2}$ λ7377.00 is too far away, while a O II λ7367.68 identification is doubtful given its high upper level energy. The C V 7p $^3P^o$–8d ^3D λ7367.60 transition is a possible alternate identification, but only one other C V transition in the spectrum, C V 6gh ^{1,3}G,H^o–7hi ^{1,3}H^o,I λ4944.50 with an IDI value of 3, is a top ranked EMILI IDI; others are of lesser rank or do not appear in the EMILI lists for the corresponding observed lines.

The other nebular transition, [Br IV] $^3P_2$–$^1D_2$ λ9450.5 was not detected by PB94, even though the line should be of the same intensity (Biémont & Hansen 1986a). Comparison between the IC 418 and NGC 7027 spectra shows that something is filling in the telluric absorption feature in the latter at 9450.85Å, with an estimated intensity close to [Br IV] λ7368.10, although a ghost feature at this wavelength arising from scattered light within the spectrograph cannot be ruled out based on the proximity of other similar features. If the feature is real, however, the alternate identification of Fe I λ9450.95 is not compelling. Therefore, both transitions are identified in NGC 7027, although tentatively since they appear in only one PN spectra, may be attributable to misinterpretation of the local continuum level complicated by telluric absorption of varying degree, and the latter observed line may be spurious. No auroral or trans-auroral features of [Br IV] were identified in any spectrum.

6.4. Other Z>30 Line Identifications

The spectra were searched for lines originating from other Z>30 ions. Among the numerous coincidences between observed lines and transition wavelengths at the ±1Å level, those listed in Table 10 were judged to be the most likely to correspond to real lines describable by a Z>30 identification in at least one of the PNe. Given the low abundances of these ions, only transitions among the lowest-lying levels were expected to be observable.

PB94 declared as certain the identification of a line at 5758.7Å in NGC 7027 as [Rb IV] $^3P_2$–$^1D_2$ λ5759.44. Corresponding lines are detected in 4 of 5 PNe here. However, at even the highest instrumental resolution, this transition would blend with He II 5–47 λ5759.74. In NGC 2440 and IC 4191 there is contamination from a flare or ghost at the position of He II 5–47 λ5759.74 in one spectral order. Using only the uncontaminated order, and inspecting the nearby He II 5–n sequence suggests that in IC 4191 the He II λ5759.74 line shows significant excess, while in NGC 2440 there is better agreement with recombination theory and the line is likely He II. The NGC 7027 spectra, taken with a different instrument, does not show any contamination, but does show a similar excess in He II 5–47 λ5759.74. Thus, the line intensities in IC 4191 and NGC 7027 were corrected by I(5–47)/I(5–46)=0.95 derived from the ratio of the their emissivities (Storey & Hummer 1995). IC 418 has no detectable He II lines, enhancing the [Rb IV] λ5759.44 identification, but the weakness and irregularity of its profile cast doubt upon its reality as a line, and it is only tentatively identified here. The alternate EMILI recommended identification, [Fe II] λ5759.30, was not considered likely given its high excitation energy. Since the expected intensity ratio of $^3P_2$–$^1D_2$ λ5759.44 to $^3P_1$–$^1D_2$ 9008.75 is 17 (Biémont & Hansen 1986b), the apparition of λ9008.75 in IC 418 and NGC 7027 is probably likely due to He I 3d ^3D–10p $^3P^o$ λ9009.23,.26, or is unreal. In summary, the [Rb IV] λ5759.55 line is identified in IC 4191, NGC 7027, and tentatively in IC 418.

Another Rb line detection considered probable by PB94 in NGC 7027 is [Rb V] $^4S^o_{3/2}$–$^2D^o_{3/2}$ λ5363.6, which they identified at 5364.2Å. Although it does not appear in the EMILI list for the corresponding lines in our spectra, we believe that its identification in at least NGC 7027 is viable given the poor multiplet statistics of [Ni IV] λ5363.35, where none of the four other multiplet lines are clearly present. The O II 4f F $^2[4]^o_{7/2}$–4d′ $^2F_{7/2}$ λ5363.80 identification is an interesting alternative. Well-known O II dielectronic doublet lines of multiplets V15, V16, and V36, such as 3s′ $^2D_{5/2}$–3p′ $^2F^o_{7/2}$ (V15) λ4590.97 are all clearly present in all of our PNe spectra, except NGC 7027 where they either outside the bandpass or not optimally placed for detection, at intensities $\sim 10^{-4}$ I(Hβ). These lines are present at similar intensities in the NGC 7027 spectrum of Zhang et al. (2005). Lines from 3d–4f transitions, particularly 3d $^2D_{5/2}$–4f F $^2[4]^o_{7/2}$ (V92a) λ4609.4 arising from the lower level of the O II λ5363.80 transition are also favorably identified at roughly the same intensity. Therefore it is not out of the realm of possibility that this line is evidence of the partial feeding of $^2[4]^o_{7/2}$ level. However, while EMILI did not perform a multiplet check on this line (due to a non LS-coupled lower level), two other transitions at 5361.74Å and 5375.57Å from the same upper term and ending on this level are not present in any of the spectra. Without

spontaneous emission coefficients it is difficult to judge a potential branching ratio for these transitions. Therefore, it is believed that [Rb IV] λ5363.60 might be tentatively identified in IC 2501 and IC 4191 as well. Unfortunately the matching $^4S^o_{3/2}$–$^2D^o_{5/2}$ λ4742.40 line is disguised by a flare or ghost in the MIKE spectra, and is not optimally placed in NGC 7027 to allow a spectroscopic confirmation, nor observed in IC 2501 and IC 4191.

Numerous lines of various Sr ions were searched for, including the strong (I/I(Hβ)=3 $\times$ 10^{-4}) [Sr IV] $^2P^o_{3/2}$–$^2P^o_{1/2}$ λ10276.9 fine-structure line named as a possible identification by PB94 in NGC 7027, [Sr VI] $^4S^o_{3/2}$–$^2D^o_{5/2}$ λ4249.2 and $^2D^o_{3/2}$–$^2P^o_{1/2}$ λ5434.3 identified as possible and tentative respectively by PB94 and also identified by Zhang et al. (2004), and the Sr II resonance lines at $\lambda\lambda$4077.71,4215.52, and the [Sr II] $^2S_{1/2}$–$^2D_{5/2,3/2}$ $\lambda\lambda$6738.39,6868.17 lines observed in η Carinae (Zethson et al. 2001). While, there were some instances of wavelength coincidences with observed lines, the magnitude of the wavelength differences and existence of plausible alternate identifications, such as [Fe II] 4249.08 for [Sr VI] λ4249.2, did not warrant a claim of identification. The same was true for Y and Zr, where the [Y V] $^2P^o_{3/2}$–$^2P^o_{1/2}$ λ8023.6 and [Zr VII] $^3P_2$–$^3P_0$ λ7961.4 fine-structure lines , listed as possible and tentative identifications by PB94 respectively, did not have any wavelength coincidence with an observed line in any PNe within the initial $\pm$1Å screening criteria.

Turning to the fifth row of the periodic table, we believe that an observed and previously unidentified line in IC 418 may correspond to [Te III] $^3P_1$–$^1D_2$ λ7933.3, which would be the first optical identification of a Te III line in a PN. The He I 3p $^3P^o$–ns ^3S sequence of lines, of which the alternate identifications He I $\lambda\lambda$7932.36,.41 are members, does not become clearly evident in this spectrum until 3p–10s at 8632.76Å and 8632.83Å. The wavelength coverage of our spectra does not extend out to the possibly stronger $^3P_2$–$^1D_2$ λ10876.0 transition, so this line cannot be used to check the Te III identification. Similarly, the detection of a possible [I III] $^4S^o_{3/2}$–$^2D^o_{3/2}$ λ8536.6 line in NGC 7027, with a less than compelling Cr II permitted line as an alternate primary EMILI identification, cannot be confirmed through observation of its companion $^4S^o_{3/2}$–$^2D^o_{5/2}$ λ6708.7 transition. The putative λ6708.7 line appears to be better explained by a combination of [Mn II] λ6709.93 and possibly [Cr V] λ6709.8, although the latter line has poor multiplet statistics (2/0). Nevertheless, the [I III] λ8536.6 transition has a definite IDI that is second ranked for its corresponding observed line, so we count this as a tentative detection for NGC 7027.

PB94 claims the detection of four transitions belonging to permitted multiplets of Ba II, with three detections considered certain, and one considered possible. Some of these same transitions have also been identified in emission by (Zhang et al. 2005) in NGC 7027 and by Hobbs et al. (2004) in the compact H II region within the Red Rectangle. In the present sample it is believed that one of the transitions considered certain by PB94, Ba II 5d $^2D_{5/2}$–6p $^2P^o_{3/2}$ λ6141.71, may correspond to an observed line in three of five PNe. Given the low solar abundance and high condensation temperature (1455 K; Lodders et al. 2003) of Ba, the detection of these transitions might initially be considered unlikely. However, as originally proposed by PB94, if sufficient gas-phase Ba^+ is available for collisional excitation, emission, and moderate self absorption, it is estimated that optical depths of 0.5 and 2.7 in the 6s

$^2S_{1/2}$–6p $^2P^o_{3/2}$ λ4554.03 resonance transition are sufficient to account for both its apparent non-detection, and for the observed intensity of the putative λ6141.71 lines in NGC 2440 and IC 4191 respectively. PB94 estimated an optical depth of 3 for the λ4554.03 transition in NGC 7027. Under these scenarios the λ6141.71 line is either among the strongest or is the strongest observable Ba II line, with its relative intensity with respect to other Ba II lines increasing with a larger optical depth in the λ4554.03 line.

The EMILI results do suggest some potentially viable alternative identifications other than Ba II for individual PN, but none that can satisfactorily account for the observed line in all three. O I 18d $^3D^o_2$–4p′ $^3D_3$ λ6141.75 arises from an auto-ionizing level, is too strong with respect to other permitted O I transitions further down the cascade chain, and is not accompanied by any other multiplet members in any PNe. Under the abundance and ionization model created by EMILI for NGC 2440 and IC 4191, Ne III 4p $^5P_3$–4d $^5D^o_4$ λ6141.48 did not produce an emission line with an intensity within three orders of magnitude of the strongest predicted intensity among all putative identifications. This was not the case in NGC 7027, where the line was among the strongest predicted lines, is expected to be the among the strongest in the multiplet, and where the identification is enhanced by favorable multiplet statistics. The [Ni III] 4s $^3F_2$–4s $^3P_1$ λ6141.83, arises from a level of high excitation energy (9.9 eV), is probably not the strongest member of its multiplet as it does not originate from the level of the multiplet with the highest statistical weight, and other potentially stronger multiplet members are not observed in IC 2501 and NGC 7027. Yet in NGC 2440, the multiplet statistics are somewhat better, and the large intensity of the corresponding observed line and the Ba abundance derived from it is at odds with lower abundances derived for Kr and Xe in subsequent abundance analysis. The excellent agreement between the observed wavelengths in *all* three PNe and the Ba II λ6141.71 wavelength, the expectation that λ6141.71 is the strongest Ba II line, and the lack of a good alternate identification for IC 4191, suggests that Ba II λ6141.71 warrants serious consideration as the correct identification in all cases.

The fine-structure transition [Ba IV] $^2P^o_{3/2}$–$^2P^o_{1/2}$ λ5696.6, another certain detection from PB94, is verified by its detection in our NGC 7027 spectrum after a correction for C III (V2) λ5695.92 is made. The intensity attributable to λ5696.6 was determined using the effective recombination coefficient for C III λ5695.92 ($\alpha = 3.1 \times 10^{-15}$ cm^3 s^{-1}) specified by PB94, those from Nussbaumer & Storey (1984) and Péquignot, Petitjean, & Boisson (1991) for C III 5g ^{1,3}G–6h $^{1,3}H^o$ λ8196.61, and the λ8196.61 line's observed intensity. Subtraction yielded a line amounting to 36% of the originally observed intensity.

The only sixth-row elemental transition sought in these spectra was the fine-structure [Pb II] $^2P^o_{1/2}$–$^2P^o_{3/2}$ λ7099.80 line, which was identified with certainty by PB94. The transition appears in the EMILI list for IC 418 tied for the highest ranked transition for a previously unidentified line. For NGC 7027, the transition is not ranked, but the competing identifications in its EMILI list are not convincing given their high excitation energies. Excellent wavelength agreement is seen in both cases, and both identifications are considered certain.

In summary, of the 18 Z>30 elemental ion transitions considered certain or probable

by PB94 in NGC 7027, 15 are believed to be detected to various degrees of certainty in the present set of spectra. The final intensities of all Z>30 lines detected with any certainty within at least one PN are presented in Table 11, with certain identification listed in bold, and tentative identifications in normal type. Conspicuous among those missing from PB94 is [Se III] $^3P_1$–$^1D_2$ λ8854.2. The nearby He I 3d ^3D–11p $^3P^o$ λ8854.14 transition does appear to show a large excess relative to that expected from other confirmed lines in the same series in both IC 418 and IC 7027. However, the energy levels in the Atomic Line List v2.05, derived from Moore (1952) and also utilized by PB94, have a listed uncertainty of 6.3 cm^{-1} that exceeds the maximum 1 cm^{-1} tolerance allowed for inclusion of supplemental Z>36 ions into EMILI. This leads to an error of up to 10Å in the transition wavelength. Thus, the identification cannot be confirmed under the present degree of energy level uncertainty. Also missing are the Ba II transitions 6s $^2S_{1/2}$–6p $^2P^o_{3/2}$ λ4554.03 and 5d $^2D_{3/2}$–6p $^2P^o_{3/2,1/2}$ $\lambda\lambda$5853.67,6496.90. As discussed previously, all would be weaker in our spectra than the potentially observed λ6141.71 under the assumption of a moderate optical depth in the resonance transition λ4554.03 (and 6s $^2S_{1/2}$–6p $^2P^o_{1/2}$ λ4934.08 not observed by PB94).

Zhang et al. (2005) has claimed the identification of 5 additional transitions in their NGC 7027 spectra belonging to Z>30 elements that were not observed in our spectra. Two additional permitted Ba II lines, Ba II λ4554.03 and Ba II λ4934.08 are detected, both weaker than the λ6141.71 line as would be expected for substantial optical depths of the resonance lines. They also identify auroral [Br III] λ7385.2 and [Rb V] λ5080.2, although the nebular [Br III] λ6131.0 and [Rb V] $\lambda\lambda$4742.4,5363.6 lines, which might be expected to be stronger than the auroral lines, are not identified. Zhang et al. (2005) also identifies [Sr VI] λ4249.2, which might be better attributable to [Fe II] λ4249.08.

6.5. Z>30 Line Identifications in H II Regions

In comparing the spectra of the PNe with H II regions, we note that no post-Fe peak lines were identified by García-Rojas et al. (2004) in their deep VLT UVES echelle spectrum of the H II region NGC 3576. In Table 11 are included estimates of the upper limits to undetected Kr and Xe line intensities for this H II region from the faintest detectable lines that were identified at neighboring wavelengths or from artificial lines inserted at their wavelengths that meet minimal detection S/N statistics. In the spectrum of the Orion Nebula, Baldwin et al. (2000) reported weak (I$\approx 2\times10^{-5}$ Hβ) unidentified features at 5867.8 Å and 6826.9 Å that were originally unidentified, but can now be positively identified as [Kr IV] $^4S^o_{3/2}$–$^2D^o_{3/2}$ λ5867.74 and [Kr III] $^3P_2$–$^1D_2$ λ6826.70 respectively. However, there are no other close coincidences between any lines listed in Tables 7–10, except for 5363.34Å which would correspond with [Rb V] $^4S^o_{3/2}$–$^2D^o_{3/2}$ λ5363.60, an unlikely identification given the unrealistically high degree of ionization (40 eV) for an H II region. The observed intensities and upper limits are also included in Table 11.

7. Z>30 Abundances

The line intensities given in Table 11 were used to compute abundances for Ba, Kr, Xe, and Br ions. The atomic data listed in Table 3 were formatted for inclusion in 5-level atom models for abundance analysis with the IRAF *nebular* task *abundance*, or for the cases of the fine structure lines [Xe VI] λ6408.9 and [Ba IV] λ5696.6, using a two-level atomic solution code. For the [Br III] and [Br IV] lines the relevant collision strengths have not yet been calculated. However, since these ions are isoelectronic with [Kr IV] and [Kr V], and because collision strengths for the same levels along an isoelectronic sequence tend to vary with effective nuclear charge (Seaton 1958), with some exceptions, the collision strengths of [Br III] and [Br IV] were assumed to be 25% smaller than those for Kr. Because collision strengths were not calculated by Schöning & Butler (1998) for [Xe V] transitions, the [Kr V] collision strengths for the same transitions were utilized in the Xe^{+4} analysis. Collision strengths for excitation to the $^3P_2$ parent level of the tentatively observed [Xe V] $5p^2\ ^3P_0$–$^3P_2$ λ7076.8 line in other np^2 ions such as Ne V (Lennon & Burke 1994), Ar V (Galavis, Mendoza, & Zeippen 1995), and Kr V (Schöning 1997), depart by 15% at most from their Kr V values at 10000 K. The temperatures and densities used for these analyses corresponded to those from diagnostics with the closest ionization potential. The [Ar III] (27.6 eV) temperature and [Cl III] (23.8 eV) density diagnostic values were used for [Br III] (21.8 eV), [Kr III] (24.4 eV), [Xe III] (21.1 eV), and [Ba IV] (20.0 eV); [O III] (35.1 eV) temperature and [Ar IV] (40.1 eV) density for [Br IV] (36.0 eV), [Kr IV] (37.0 eV), and [Xe IV] (32.1 eV); [Ne III] (41.0 eV) temperature [Ar IV] (40.1 eV) density for [Xe IV] (46.0 eV); [Ar V] (59.8 eV) temperature and [K V] (60.9 eV) density for [Kr V (52.5 eV)] and [Xe VI] (57.0 eV). The [O I] temperature and [N I] density were used for Ba II assuming collision excitation of Ba^+ as the source of Ba II λ6141.71. Averaged diagnostic values were used when one of the diagnostics was unavailable for a particular ion. Uncertainties were computed in the same manner as the lighter elements, through permutation of intensity measurement and diagnostic value errors, where available, and selection of extrema values. For lines that were corrected for blending, 25% of the value of the correction was added to the measurement uncertainty.

Table 12 presents the results of the abundance determinations for individual lines of Ba, Br, Kr, and Xe ions. To compute overall elemental abundances for the latter three ions, argon has been selected as a benchmark element in addition to hydrogen. This was done because the ionization potentials of the noble gases Ar, Kr, and Xe, as well as Br, are very similar for their first three stages of ionization and therefore ionization corrections should not be large when making abundance comparisons among these elements. Additionally, the noble gases are almost completely non-reactive and have very low condensation temperatures, so corrections for gas phase abundances depleted by grain formation are insignificant for these elements. Only ionic abundances relative to hydrogen were computed for Ba.

We convert from ionic to elemental abundances by making use of the similarity in

ionization potentials of the noble gases, so that

$$\begin{aligned} \mathrm{Kr/Ar} &= (\mathrm{Kr^{+2}} + \mathrm{Kr^{+3}})/(\mathrm{Ar^{+2}} + \mathrm{Ar^{+3}}) \,\mathrm{and}\, (\mathrm{Kr^{+2}} + \mathrm{Kr^{+3}} + \mathrm{Kr^{+4}})/(\mathrm{Ar^{+2}} + \mathrm{Ar^{+3}} + \mathrm{Ar^{+4}})\,, \\ \mathrm{Xe/Ar} &= (\mathrm{Xe^{+2}} + \mathrm{Xe^{+3}})/(\mathrm{Ar^{+2}} + \mathrm{Ar^{+3}}) \,\mathrm{and}\, (\mathrm{Xe^{+2}} + \mathrm{Xe^{+3}} + \mathrm{Xe^{+4}} + \mathrm{Xe^{+5}})/(\mathrm{Ar^{+2}} + \mathrm{Ar^{+3}} + \mathrm{Ar^{+4}})\,, \end{aligned}$$

for H II regions and PNe judged to be of low excitation (IC 2501 and IC 418), and for high-excitation PNe (NGC 2440, IC 4191, NGC 7027), respectively. The Kr^{+4}/H^{+} abundance was included in the IC 2501 Kr/Ar ratio determination. For NGC 7027, the Br/Ar ratio was calculated the same way as the Xe/Ar ratio, with corrections for unobservable Br^{+4} and Br^{+5} made assuming Br^{+4},Br^{+5}/Br=Xe^{+4},Xe^{+5}/Xe, appropriate because of their very similar ionization potentials.

The resulting abundances are listed in the bottom rows of Table 12 relative to their solar values from Lodders (2003). Three particular results are noteworthy. First, three out of five PNe show significant enhancements in Kr and Xe relative to solar values, while two others show similar, solar-like values. It is also interesting to note that IC 418 and NGC 7027, both considered young PNe, have the largest over-abundances, although they are of greatly different ionization classes. Meanwhile, the H II regions show only solar Kr abundances, indicative of unprocessed ISM gas. Secondly, the Kr and Xe abundances in all PNe all show enhancements of similar magnitude, as was seen in NGC 7027 by PB94. Finally, for NGC 7027, the Br abundance also shows a level of enhancement similar to that of Kr and Xe. Uncertainties remain regarding the adaptability of Kr collision strengths, modified as was done here, for the Br abundance calculations. However, to reduce the Br abundance to solar, the collisions strengths for Br^{+2} and Br^{+3} would have to both be four times greater than their counterparts in Kr, and this is much larger than the difference seen for analogous transitions for other p^2 and p^3 ion pairs (N and O, Cl and Ar). In any event, the prevalence of probable Br line identifications suggests, independent of the actual atomic data, that significant Br does exists in most of the PN comprising our sample.

It is of interest to compare the s-process abundances we derive for PNe with those obtained for evolved stars from analyses of their absorption spectra. With the exception of Rb, Ba, and Pb, the elements observed in emission in PNe are different from those normally observed in the spectra of late-type stars, so a direct comparison is not feasible. In fact, lines of the same *s*-process elements are not necessarily even observed in similar-type stars. For this reason Luck et al. (1991) defined two parameters, [ls] and [hs], that represent the mean abundance of elements associated with Sr and Ba, respectively, in what are called the "light" and "heavy" *s*-process peaks. They define the abundance indices [ls] and [hs] for an object as the mean logarithmic abundances relative to iron of (Y, Zr, & Sr) and (Ba, Nd, La, & Sm), respectively, compared to their solar mean abundances. All of these elements are produced by the *s*-process, although several of them have predominantly *r*-process contributions for solar-type stars (Arlandini et al. 1999).

Of the post-Fe peak elements that are observed in PNe, Kr belongs to the light *s*-process peak near Sr, and Xe is near Ba in the heavy *s*-process peak. Both are produced by the *s*-process, although Xe is predominantly an *r*-process element for stars of solar metalicity.

Using models to determine the appropriate correction factors, Kr and Xe can be incorporated into the [ls] and [hs] indices. However, in making comparisons of nebular abundances with those derived from stellar spectra Fe should not be used as the fiducial abundance for nebulae because its consistently strong depletion from the gas phase due to grain formation causes its true abundance in nebulae to be indeterminate (Shields 1975; Perinotto et al. 1999). Argon is a good surrogate for Fe because it does not suffer depletion in nebulae, and it is well observed in nebulae in multiple ionization stages and the relevant excitation cross sections are known.

The extent to which *s*-process nucleosynthesis occurs in stars is determined by the total neutron exposure after the Third Dredge Up phase. Calculations show that neutron exposure is the primary factor that determines the ratio of the enhancements of the heavy to light *s*-process elements, i.e., [hs/ls], the "neutron-exposure-related-parameter". Low neutron exposures result in element production confined to a crowded region around the Sr peak, producing [hs/ls]< 0, whereas higher neutron exposures significantly populate the Ba peak, leading to [hs/ls]>0 (Busso et al. 1995; Busso, Gallino, & Wasserburg 1999). The fact that [Xe/Kr]$\approx$1 for PNe, in spite of Xe not being produced by the s-process as much as Kr, is strongly suggestive that the progenitor AGB stars of PNe experience significant neutron exposure. Of equal significance, the fact that forbidden lines of post-Fe peak elements not observed in stars are detectable in nebulae causes H II regions and PNe to be of potentially great value in studying the nucleosynthesis of these elements.

8. Summary

In summary, very high signal-to-noise spectra of PNe do reveal lines from elements that are enhanced by the *s*-process, as was also found by other investigators. Because many post-Fe peak elements are refractory their gas phase abundances are not reliable indicators of the nucleosynthetic processes that have occurred in the progenitor stars. Fortunately, the noble gases Ar, Kr, and Xe are largely unaffected by molecular and grain formation, and the latter two elements are situated in the light and heavy *s*-process peaks, respectively. They also have easily excitable and observable lines in multiple ionization stages for which atomic cross sections are now available, and whose analyses should be straightforward.

We find for a sample of five PNe that Kr and Xe abundances are enhanced over solar values by up to an order of magnitude, from both an analysis of their intensities relative to those of the fiducial element Ar, and also from a relative comparison of their line strengths in PNe vs. H II regions such as the Orion Nebula, where the lines are very weak in gas that is representative of the ISM composition. The similar enhancements of Kr and Xe in PNe are suggestive of large neutron exposures in the progenitor central stars. Further spectroscopy of PNe should reveal additional post-Fe peak emission lines whose analyses will contribute to a more complete picture of post-main sequence stellar evolution, while deep spectra of H II regions should lead to improved values of the ISM abundances of these elements

The work of YZ and XWL was partially supported by Chinese NSFC Grant NO.10325312, and YZ gratefully acknowledges the award of an Institute Fellowship from STScI, where his work was carried out. EP, KC, and JAB gratefully acknowledge support for this work from NSF grant AST-0305833 and HST grant GO09736.02-A.

REFERENCES

Arlandini, C., Kappeler, F., Wisshak, K., Gallino, R., Lugaro, M., Busso, M., & Straniero, O. 1999, ApJ, 525, 886

Baldwin, J. A., Verner, E. M., Verner, D. A., Ferland, G. J., Martin, P. G., Korista, K. T., & Rubin, R. H. 2000, ApJS, 129, 229

Baluteau, J.-P., Zavagno, A., Morisset, C. & Péquignot, D. 1995, A&A, 303, 175

Benjamin, R. A., Skillman, E. D., & Smits, D. P. 1999, ApJ, 514, 307

Biémont, E., & Hansen, J. E. 1986a, Phys. Scr. 33, 117

Biémont, E., & Hansen, J. E. 1986b, Phys. Scr. 34, 116

Biémont, E., Cowan, R.D., & Hansen, J.E. 1988, *Phys. Scr.*, 37, 850

Biémont, E., Hansen, J. E., Quinet, P., & Zeippen, C. J. 1995, A&A, 333, 34 6

Barge, T., Wahlgren, G.M., Johansson, S.G., Leckrone, D.S., & Proffitt, C.R. 1998, ApJ, 496, 1051

Busso, M., Lambert, D. L., Beglio, L., Gallino, R., Raiteri, C. M., & Smith, V. V. 1995, ApJ, 446, 775

Busso, M., Gallino, R., Wasserburg, G. J. 1999, ARA&A, 37, 239

Cahn, J. H., Kaler, J. B., & Stanghellini, L. 1992, A&AS, 94, 399

Churilov, S.S. & Joshi, Y.N. 2000, *Phys. Scr.*, 62, 358

Churilov, S.S., Joshi, Y.N., & Gayasov, R. 2002, *J. Opt. Soc. Amer. B*, 18, 113

Cosby, P.C. & Slanger, T.G. 2006, *Can. J. Phys.*, in press

Cosby, P. C., Sharpee, B. D., Slanger, T. G., & Huestis, D. L. 2006, J. Geophys. Res., in press

Davey, A.R., Storey, P.J., & Kisielius, R. 2000, A&AS, 142, 85

Dinerstein, H. L. 2001, ApJ, 550, L223

Esteban, C., Peimbert, M., García-Rojas, J., Ruiz, M.T., Peimbert, A., & Rodríguez, M. 2004, MNRAS, 355, 229

Froese Fischer, C. & Tachiev, G. 2004, *At. Data Nucl. Data Tab.*, 87, 1

Galavis, M.E., Mendoza, C., & Zeippen, C.J. 1995, A&AS, 111, 347

Gallard, M., Raineri, M., Reyna Almandos, J.G., Sobral, H., & Callegari, F. 1999, *J. Quant. Spec. Rad. Trans.*, 61, 319

García-Rojas, J., Esteban, C., Peimbert, M., Rodríguez, M., Ruiz, M.T., & Peimbert, A. 2004, ApJS, 153, 501

Gurzadyan, G. A. 1997, The Physics and Dynamics of Planetary Nebulae (Berlin: Springer)

Hamuy,M., Suntzeff,N.B., Heathcote,S.R., Walker,A.R., Gigoux,P. & Phillips,M.M. 1994, PASP, 106,566

Hansen, J.E. & Persson, W. 1974, *J. Opt. Soc. Amer.*, 64, 696

Hansen, J.E. & Persson, W. 1976, *Phys. Scr.*, 13, 166

Hanuschik, R. W. 2003, A&A, 407, 1157

Hobbs, L. M., Thorburn, J. A., Oka, T., Barentine, J., Snow, T. P., & York, D. G. 2004, ApJ, 615, 947

Howarth, I.D. 1983, MNRAS, 203, 301

Hyung, S., Keyes, C.D., Aller, L.H. 1995, MNRAS, 272, 49

Hyung, S., Aller, L.H., Feibelman, W.A., & Lee, S.-J. 2001, ApJ, 563, 889

Jaschek, C., & Jaschek, M. 1995,"The Behavior of Chemical Elements in Stars" (Cambridge University Press: Cambridge)

Joshi, Y.N., Tauheed, A., & Davison, I.G. 1992, *Can. J. Phys.*, 70, 740

Karlsson, H. & Litzén, U. 1999, *Phys. Scr.*, 60, 321

Kaufman, V., Sugar, J., & Joshi, Y.N. 1988, *J. Opt. Soc. Amer. B*,5, 619

Kingdon, J. & Ferland, G.J. 1995, ApJ, 442, 714

Kisielius, R. & Storey, P.J. 2002, A&A, 387, 1135

Kisielius, R., Storey, P.J., Davey, A.R., & Neale, L.T. 1998, A&AS, 133, 257

Klose, J.Z., Fuhr, J.R., & Weise, W.L. 2002, *J. Phys. Chem. Rev. Data*, 31, 217

Lennon, D.J. & Burke, V.M. 1994, A&AS, 103, 273

Liu, X.-W. 2004, in Planetary Nebulae beyond the Milky Way, eds. J. Walsh, L. Stanghellini and N. Douglas (ESO, Garching bei München), in press

Liu, X.-W., Storey, P. J., Barlow, M. J., Danziger, I. J., Cohen, M.,& Bryce, M. 2000, MNRAS, 312, 585

Lodders, K. 2003, ApJ, 591, 1220

Luck, R.E. & Bond, H.E. 1991, ApJS, 77, 515

Mendoza, C. 1983, in Planetary Nebulae; Proceedings of the Symposium, London, England, August 9-13, 1982, ed. D.R. Flower, (Dordrecth, D. Rediel Publishing Co.), 143

Moore C.E. 1952, Atomic Energy Levels, Vol. II - NBS Circ. 467, Washington, DC

Moore C.E. 1958, Atomic Energy Levels, Vol. III - NBS Circ. 467, Washington, DC

Nussbaumer, H. & Storey, P. J. 1984, A&AS, 56, 293

Osterbrock, D. E. & Ferland, G. J. 2006, *Astrophysics of Gaseous Nebulae and Active Galactic Neclei*, (Mill Valley: University Science Books)

Osterbrock, D. E., Fulbright, J. P., Martel, A. R., Keane, M. J., & Trager, S. C. 1996, PASP, 108, 277

Peimbert, M., Peimbert, A., Ruiz, M. T., & Esteban, C. 2004, ApJS, 150, 431

Péquignot, D., & Baluteau, J. P. 1994, A&A, 283, 593

Péquignot, D., Petitjean, P., & Boisson, C. 1991, A&A, 251, 680

Perinotto, M. 1991, ApJS, 76, 687

Perinotto, M., Bencini, C.G., Pasquali, A., Manchado, A., Rodríguez Espinosa, J.M., & Stanga, R. 1999, A&A, 347, 967

Persson, W. & Petterson, S.-G. 1984, *Phys. Scr.*, 29, 308

Persson, W. & Wahlstrom, C.-G. 1985, *Phys. Scr.*, 31, 487

Persson, W. & Reader, J. 1986, *J. Opt. Soc. Amer. B*, 3, 959

Persson, W., Wahlstrom, W.-G., Bertuccelli, G., DiRocco H.O., Reyna Almandos, J.G., & Gallardo, M. 1988, *Phys. Scr.*, 38, 347

Reader, J. 1983, *J. Opt. Soc. Amer.*, 73, 349.

Reader, J. & Acquista, N. 1976, *J. Opt. Soc. Amer.*, 66, 896

Reader, J. & Epstein, G.L. 1972, *J. Opt. Soc. Am.*, 62, 619

Robertson-Tessi, M. & Garnett, D.R. 2005, ApJS157, 371

Rodríguez, M. 2003, ApJ, 590, 296

Safronova, U.I., Safronova, M.S., & Johnson, W.R. 2005, *Phys. Rev. A.*, 71, 052506

Sansonetti, C.J., Reader, J., Tauheed, A., & Yoshi, Y.N. 1993, *J. Opt. Soc. Am. B*, 10, 7

Schöning, T. 1997, A&A, 122, 277

Schöning, T., & Butler, K. 1998, A&A, 128, 581

Seaton, M. J. 1958, *Rev. Mod. Phys.*, 30, 979

Sharpee, B., Williams, R., Baldwin, J. A., & van Hoof, P.A.M. 2003, ApJS, 149, 157

Sharpee, B., Baldwin, J. A., & Williams, R. 2004, ApJ, 615, 323

Shaw, R. A. & Dufour, R. J. 1995, PASP, 107, 896

Shields, G.A. 1975, ApJ, 195, 475

Simmerer, J., Sneden, C., Cowan, J. J. et al. 2004, ApJ, 617, 1091

Smits, D. P. 1991, MNRAS, 251, 316

Smits, D. P. 1996, MNRAS, 278, 683

Sterling, N. C. & Dinerstein, H. L. 2003, Rev.Mex.Ast. & Ap.Ser.Conf. 18, p. 133

Sterling, N. C. & Dinerstein, H. L. 2004, in ASP Conf. Ser. 313, Asymmetric Planetary Nebulae III, ed. M. Meixner, J. Kastner, B. Balick, & N. Soker (San Francisco: ASP), p. 410

Sterling, N. C., Dinerstein, H. L., & Bowers, C. W. 2002, ApJ, 578, L55

Storey, P.J. 1994, A&A, 282, 999

Storey, P. J. & Hummer, D. G. 1995, MNRAS, 272, 41

Tauheed, A. & Joshi, Y.N. 1992, *Phys. Scr.*, 46, 403

Tauheed, A. & Joshi, Y.N. 1993a, *Phys. Scr.*, 47, 550

Tauheed, A. & Joshi, Y.N. 1993b, *Phys. Rev. A.*, 47, 3092

Tauheed, A., Joshi, Y.N., & Kaufman, V. 1991, *Phys. Scr.*, 44, 579

Tauheed, A., Joshi, Y.N., & Pinnington, E.H. 1993, *Phys. Scr.*, 47, 555

Wesson, R., Liu, X.-W., & Barlow, M.J. 2003, MNRAS, 340, 253

Wilson, N.J. & Bell, K. L. 2002, MNRAS, 331, 389

Zethson, T., Gull, T. R., Hartman, H., Johansson, S., Davidson, K., & Ishibashi, K. 2001, AJ, 122, 322

Zhang, Y. & Liu, X. -W. 2002, MNRAS, 337, 499

Zhang, Y. & Liu, X. -W. 2003, A&A, 404,545

Zhang, Y., Liu, X. -W., Wesson, R., Storey, P. J., Liu, Y., Danziger, I. J. 2004, MNRAS, 351, 935

Zhang, Y., Liu, X. -W., Luo, S.-G., Péquignot, D., & Barlow, M. J. 2005, A&A, 442, 249

Table 1. Journal of Observations

Object	Telescope	Dates(UT)	Integration Times(sec)	Slit Center
NGC 7027	KPNO 4m	19–22 Jun 2002	34×1200s, 9×300s, 1×120s, 4×60s, 6×30s	3.5″ W, 0.5″ N
IC 2501	LCO 6.5m	12–13 Feb 2003	6×1800s, 1×300s, 4×60s	2″ E
IC 2501	LCO 6.5m	25–26 Feb 2003	15×1800s, 2×60s	2″ E
IC 4191	LCO 6.5m	12–13 Feb 2003	5×1800s, 1×1200s, 1×300s,1×60s	2″ E
IC 4191	LCO 6.5m	25–26 Feb 2003	10×1800s,1×300s,3×60s	2″ E
NGC 2440	LCO 6.5m	12–13 Feb 2003	11×1800s, 1×300s, 1×60s	14″ E

Table 2. Nebular Parameters

Parameter	NGC 2440	IC 2501	IC 4191	NGC 7027
V(geo) (km s^{-1})	+66.7	+23.2	−40.1	−7.1
c(Hβ)	0.55	0.55	0.77	1.17

Table 3. Electron Temperatures and Densities

Diagnostic	NGC 2440	IC 2501	IC 4191	NGC 7027
Density (cm^{-3})				
[N I] λ5198/λ5200	3300^{+2700}_{-1300}	$21000^{\cdots}_{-15000}$	$12000^{\cdots}_{-7000}$	$15000^{\cdots}_{-8000}$
[S II] λ6716/λ6731	3100^{+1200}_{-700}	11000	···	···
[O II] λ3726/λ3729[a]	3300^{+1100}_{-800}	11000^{+9000}_{-4000}	9000^{+6000}_{-3000}	···
[b]	3700	11000	···	···
[Cl III] λ5517/λ5537	4700^{+1100}_{-900}	8500^{+2100}_{-1600}	12000^{+3000}_{-2000}	47400^{+1900}_{-1800}
[Ar IV] λ4711/λ4741[c]	6200^{+1600}_{-1300}	9300^{+2100}_{-1600}	11800^{+2300}_{-1900}	···
[d]	5900^{+1600}_{-1300}	7400^{+2200}_{-1500}	11000^{+2400}_{-1800}	49200^{+1300}_{-1200}
[e]	6300^{+1600}_{-1300}	9900^{+2200}_{-1700}	13000^{+3000}_{-2000}	···
[K V] λ4123/λ4163	43000^{+19000}_{-13000}	···	41000^{+17000}_{-11000}	···
Temperature (K)				
[O I] (λ6300+λ6464)/λ5577	9400±300	6900^{+300}_{-200}	7900^{+500}_{-300}	11300^{+300}_{-200}
[S II] (λ6716+λ6731)/(λ4068+λ4076)	15000^{+6000}_{-4000}	12000	···	···
[O II] (λ3726+λ3729)/(λ7320+λ7330)	16000	13000	···	···
[N II] (λ6548+λ6583)/λ5755	12600^{+700}_{-600}	10800^{+900}_{-1100}	12500±1100	···
[Ar III] (λ7136+λ7751)/λ5192	13100^{+700}_{-600}	9400^{+600}_{-500}	13000^{+800}_{-600}	12900±200
[O III] (λ4959+λ5007)/λ4363	14700^{+600}_{-500}	9500^{+300}_{-200}	9900±300	···
[Cl IV] (λ7531+λ8046)/λ5323	12900^{+1000}_{-700}	6100^{+900}_{-500}	8600^{+500}_{-400}	13700±200
[Ne III] (λ3869+λ3968)/λ3343	15500^{+500}_{-400}	11000±200	11600^{+300}_{-200}	···
[Ar V] (λ6435+λ7005)/λ4625	16400^{+1500}_{-1100}	···	11600^{+1400}_{-900}	···
Balmer/Paschen (NGC 7027) Jump	11000	7000	8000	8000

[a]Versus [O II] temperature diagnostic.

[b]Versus [N II] temperature diagnostic.

[c]Versus [O III] temperature diagnostic.

[d]Versus [Cl IV] temperature diagnostic.

[e]Versus [Ne III] temperature diagnostic.

Table 4. Ionic Abundances [a]

X^{+i}/H^+	NGC 2440	IC 2501	IC 4191	NGC 7027
Collisionally Excited Lines				
N^o/H^+	$7.25^{+0.21}_{-0.16}$	$6.9^{....}_{-0.5}$	$6.4^{....}_{-0.4}$	$6.1^{....}_{-0.3}$
N^+/H^+	$7.85^{+0.05}_{-0.06}$	$7.02^{+0.16}_{-0.10}$	$6.74^{+0.12}_{-0.09}$	7.19
O^o/H^+	$7.76^{+0.06}_{-0.05}$	$7.68^{.....}_{-0.14}$	$7.34^{.....}_{-0.11}$	$7.28^{.....}_{-0.04}$
O^+/H^+	7.24	7.30	$7.5^{+0.3}_{-0.2}$	7.68
O^{+2}/H^+	$8.26^{+0.04}_{-0.05}$	$8.59^{+0.04}_{-0.05}$	8.79±0.05	8.44
Ne^{+2}/H^+	$7.41^{+0.03}_{-0.04}$	7.58±0.03	$7.79^{+0.03}_{-0.04}$	···
S^+/H^+	5.5±0.3	5.93	5.67	5.80
S^{+2}/H^+	$6.23^{+0.07}_{-0.08}$	$6.58^{+0.11}_{-0.12}$	$6.08^{+0.07}_{-0.09}$	6.32±0.02
Cl^+/H^+	···	3.43	3.18	3.94
Cl^{+2}/H^+	4.70±0.06	$4.92^{+0.09}_{-0.10}$	$4.56^{+0.07}_{-0.08}$	4.76±0.02
Cl^{+3}/H^+	$4.69^{+0.06}_{-0.07}$	$4.66^{+0.15}_{-0.21}$	$5.23^{+0.06}_{-0.07}$	4.72±0.02
Ar^{+2}/H^+	6.13±0.04	6.27±0.07	$5.70^{+0.05}_{-0.06}$	6.09±0.02
Ar^{+3}/H^+	5.70±0.03	4.75±0.03	$5.74^{+0.03}_{-0.04}$	5.77±0.02
Ar^{+4}/H^+	$5.24^{+0.06}_{-0.08}$	···	$4.57^{+0.09}_{-0.12}$	5.60
K^{+4}/H^+	$4.59^{+0.09}_{-0.11}$	···	$3.77^{+0.14}_{-0.17}$	···
Recombination Lines				
He^+/H^+	10.86	11.04	11.00	10.81
He^{+2}/H^+	10.72	10.61	10.08	10.60
C^{+2}/H^+	8.65	8.91	8.46	8.84
N^{+2}/H^+	8.43	8.04	8.28	7.89
O^{+2}/H^+	8.51	8.69	9.08	8.46
Ne^{+2}/H^+	8.08	8.26	8.76	···

[a]In units of 12+log(X/H).

Table 5. Atomic Data for Z>30 Ions

Ion	Levels	Transition Probabilities	Collision Strengths
Br III	ALL 2.05 Biémont & Hansen (1986a) (2, 3)	Biémont & Hansen (1986a)	···
Br IV	ALL 2.05	Biémont & Hansen (1986a)	···
Kr III	ALL 2.05	Biémont & Hansen (1986b)	Schöning (1997)
Kr IV	ALL 2.05	Biémont & Hansen (1986a)	Schöning (1997)
Kr V	ALL 2.05	Biémont & Hansen (1986a)	Schöning (1997)
Rb IV	Persson & Wahlstrom (1985)	Biémont & Hansen (1986b)	···
Rb V	Persson & Petterson (1984)	Biémont & Hansen (1986a)	···
Sr II	Moore (1952)	Brage et al. (1998) (5-1, 5-2)	···
Sr IV	Hansen & Persson (1976)	Biémont, Cowan, & Hansen (1988)	···
Sr V	Hansen & Persson (1974)	Biémont & Hansen (1986b)	···
Sr VI	Persson & Petterson (1984)	Biémont & Hansen (1986a)	···
Y V	Reader & Epstein (1972)	Biémont, Cowan, & Hansen (1988)	···
Y VI	Persson & Reader (1986)	Biémont & Hansen (1986b)	···
Zr VII	Reader & Acquista (1976)	Biémont & Hansen (1986b)	···
Te III	Joshi, Tauheed, & Davison (1992)	Biémont et al. (1995)	···
I III	Tauheed & Joshi (1993b)	Biémont et al. (1995)	···
I V	Kaufman, Sugar, & Joshi (1988)	Biémont et al. (1995)	···
Xe III	Persson et al. (1988)	Biémont et al. (1995)	Schöning & Butler (1998)
Xe IV	Tauheed, Joshi, & Pinnington (1993)	Biémont et al. (1995)	Schöning & Butler (1998)
Xe V	Gallard et al. (1999)	Biémont et al. (1995)	···
Xe VI	Churilov & Joshi (2000)	Biémont et al. (1995)	Schöning & Butler (1998)
Cs V	Tauheed & Joshi (1993a)	Biémont et al. (1995)	···
Cs VI	Tauheed, Joshi, & Kaufman (1991)	Biémont et al. (1995)	···
Ba II	Karlsson & Litzén (1999)	Klose, Fuhr, & Weise (2002)	Schöning & Butler (1998)

Table 5—Continued

Ion	Levels	Transition Probabilities	Collision Strengths
Ba IV	Sansonetti et al. (1993)	Biémont et al. (1995)	Schöning & Butler (1998)
Ba V	Reader (1983)	Biémont et al. (1995)	···
Ba VII	Tauheed & Joshi (1992)	Biémont et al. (1995)	···
Ba VIII	Churilov, Joshi, & Gayasov (2002)	Biémont et al. (1995)	···
Pb II	Moore (1958)	Safronova, Safronova, & Johnson (2005)	···

Table 6. Emission Line Identifications and Intensities

$\lambda_{\rm obs}^{\rm corr}$(Å)	FWHM(km s^{-1})	$F_{\rm obs}$	$F_{\rm corr}$	S/N	Line Identification	Notes[a]
			IC 2501			
3315.23	23.73	0.0088	0.0200	7.2	[Mn III] 3315.01	:?
3323.75	19.16	0.0116	0.0260	13.9	Ne II 3323.73	
3327.17	27.98	0.0087	0.0190	10.4	Ne II 3327.15	
3328.69	19.13	0.0056	0.0130	8.4	N II 3328.72	
3334.83	18.57	0.0529	0.1200	50.0	Ne II 3334.84	
3340.81	13.75	0.0188	0.0420	13.3	N II 3340.87	
3342.64	45.56	0.0527	0.1200	37.0	[Ne III] 3342.54	
3353.22	33.40	0.0071	0.0160	11.5	[Cl III] 3353.21	
...	...	...	...	...	...	
7507.48	22.85	0.0048	0.0027	13.6	N I 7507.61	:
7509.97	57.84	0.0033	0.0019	7.1		
7512.69	52.14	0.0044	0.0025	7.1	He I 7513.33	
7514.36	36.15	0.0038	0.0022	10.7	C III 7514.30	
7515.77	22.81	0.0173	0.0099	32.2	O III 7715.99	
7530.42	29.59	0.5710	0.3300	627.6	[Cl IV] 7530.80	
7534.70	30.21	0.0022	0.0013	7.1	[Xe IV] 7535.44	

Note. — The complete version of this table is in the electronic edition of the Journal. The printed edition contains only a sample.

[a]: = uncertain identification; ? = uncertain feature; bl = line blend; ns = blend with night-sky line.

Table 7. Possible Krypton Line Identifications

Transition	NGC 2440				IC 2501				IC 4191				NGC 7027				IC 418				Ref	Notes
	λ_o, $I/I_{H\beta}$[a]	δV[b] (km s^{-1})	Mult[c]	IDI[d]	λ_o, $I/I_{H\beta}$	δV (km s^{-1})	Mult	IDI	λ_o, $I/I_{H\beta}$	δV (km s^{-1})	Mult	IDI	λ_o, $I/I_{H\beta}$	δV (km s^{-1})	Mult	IDI	λ_o, $I/I_{H\beta}$	δV (km s^{-1})	Mult	IDI		
[Kr III] 4p^4 ^{3}P$_2$–4p^4 ^{1}D$_2$ λ6826.70	6826.74	1.8	0/0	5A	6826.82	5.3	0/0	5Abl	6826.39?	-13.6	0/0	6B:	6826.91	9.2	···	··bl	6826.87	7.5	0/0	5Abl		e,*f*
C I 3p ^{1}P$_1$–4d ^{1}D$^o_2$ (V21) λ6828.12	1.0(-5)	-60.6	···	···	4.6(-5)	-57.1	···	···	1.5(-5)	-76.0	···	···	5.7(-4)	-53.2	···	···	3.3(-4)	-54.9	···	···	B95,Z05	
He I 3s ^{3}S$_1$–16p ^{3}P^o λ6827.88		-50.1	0/0	···	*2.5(-5)*	-46.6	0/0	···		-65.5	0/0	···	*4.6(-4)*	-42.6	0/0	··bl	*3.2(-4)*	-44.4	···	···	B95	
[Fe IV] 3d^5 ^{4}P$_{1/2}$–3d^5 ^{2}D5$_{3/2}$ λ6826.50		10.5	4/0	5A		14.1	4/0	5A		-4.8	4/1	3A		18.0	4/0	7A		16.3	4/0	7C		
Fe II c4F$_{7/2}$–y2G$^o_{9/2}$ λ6826.79		-2.2	4/0	6C		14.1	4/0	6C		-17.6	4/0	9D		5.3	4/0	7A		3.5	4/0	6B		
SKY: OH 7-2 R$_1$(3.5) λ6827.46		···	···	···		-4.8	···	··bl		···	···	···		12.7	···	··bl		···	···	··bl		
SKY: OH 7-2 R$_1$(4.5) λ6828.47		-9.2	···	···*		···	···	···		···	···	···		···	···	···		-1.8	···	···		
[Kr IV] 4p^3 ^{4}S$^o_{3/2}$–4p^3 ^{2}D$^o_{5/2}$ λ5346.02	5346.04	1.1	1/1	3A*	5346.07	2.8	1/1	3A*	5346.06	2.2	1/1	3A*	5345.99	-1.7	1/1	1A*	5345.94	-4.5	1/1	3A*		f
S II 4s′ ^{2}D$_{3/2}$–4p′ ^{2}F$^o_{5/2}$ (V38) λ5345.71	3.5(-4)	18.5	2/0	9	6.1(-5)	20.2	2/0	9	2.4(-4)	19.6	2/0	9	1.9(-3)	15.7	2/0	9	3.5(-5)	12.9	2/0	9	H95,P04	
C III 2s4d ^{3}D$_2$–2p3d ^{3}P$^o_1$ (V13.01) λ5345.88		9.0	5/0	7		10.7	5/0	6D		10.1	5/0	6		6.2	5/0	6		3.4	5/0	5	Z05	
[Fe II] a4F$_{3/2}$–b4P$_{3/2}$ λ5347.65		-90.3	8/0	···		-88.7	8/1	···		-89.2	8/0	···		-93.2	···	···		-96.0	···	···	ZL02	
Mg I 4s ^{3}S$_1$–9p ^{3}P^o λ5345.98		3.4	0/0	4B		5.1	0/0	4B		4.5	0/0	4B		0.6	0/0	2B		-2.2	0/0	5		
Fe II f4D$_{7/2}$–4f 2[3]$^o_{7/2}$ λ5345.95		5.1	0/0	4B		6.7	0/0	5C		6.2	0/0	5D		2.2	0/0	3C		-0.6	0/0	3A		
Si II 6p ^{2}P$^o_{3/2}$–4p′ ^{2}P$_{3/2}$ λ5346.25		-11.8	3/0	7		-10.1	3/1	6D		-10.7	3/2	4B		-14.6	3/0	8		-17.4	3/0	8		
[Kr IV] 4p^3 ^{4}S$^o_{3/2}$–4p^3 ^{2}D$^o_{3/2}$ λ5867.74	5867.68	-3.1	1/1	3A*	5867.82	4.1	1/1	4A*	5867.83	4.6	1/1	4A*	5867.71	-1.5	1/1	1A*	5867.73	-0.5	1/1	2A*		
Al II 4d ^{3}D–6f ^{3}F^o (V41) λ5867.64,.78,.89	4.6(-4)	2.0	···	···	8.5(-5)	2.0	···	···	1.9(-4)	2.6	···	···	2.6(-3)	3.6	5/0	5C	3.5(-5)	4.6	4/0	6	B00,S03	
Si II 4s′ ^{4}P$^o_{3/2}$–4p′ ^{4}P$_{1/2}$ (V48) λ5867.42		16.4	6/0	9		20.5	6/0	···		21.0	6/0	>9		14.8	6/0	8		-13.3	6/0	8	H01	
Ni II 4f 2[4]$^o_{7/2}$–7d ^{4}H$_{9/2}$ λ5867.99		-15.8	···	···		-8.7	···	···		-8.2	···	···		-14.3	0/0	7		-13.3	0/0	7	E04	
He II 5–29 5869.02		-68.5	···	···		-61.4	0/0	···		-60.8	0/0	···		-67.0	···	···		-66.0	···	···	Z05	g
[Cr III] 3d^4 ^{5}D$_3$–3d^4 ^{3}H$_5$ λ5866.97		36.3	5/0	7B		43.5	5/1	6B		44.0	5/2	4A		37.8	5/0	···		38.9	5/0	···		
Ni II 4f 2[5]$^o_{11/2}$–7d ^{2}G$_{9/2}$ λ5867.68		0.0	···	···		7.2	···	···		7.7	···	···		1.5	0/0	4B		2.6	0/0	3B		
[Kr IV] 4p^3 ^{2}D$^o_{3/2}$–4p^3 ^{2}P$^o_{3/2}$ λ6107.8	6107.68?	-5.9	···	···:	···	···	···	···	6107.50	-14.7	···	···	6107.83	1.5	3/1	5A*	···	···	···	···		
[Fe II] a6D$_{9/2}$–a2G$_{7/2}$ λ6107.28	5.6(-6)	19.6	3/0	6A:	[4.3(-6)]	···	···	···	1.9(-5)	10.8	3/0	4A:	7.2(-5)	27.0	3/0	···	[1.4(-5)]	···	···	···		
Ca I 4s7d ^{3}D$_2$–3d20p ^{3}P$^o_1$ λ6107.84		-7.9	···	···		···	···	···		-16.7	···	···		-0.5	1/0	5A		···	···	···		
Cr II c4F$_{5/2}$–4p ^{4}F$^o_{1/2}$ λ6107.96		-13.8	···	···		···	···	···		-22.6	···	···		-6.4	9/0	5A		···	···	···		
[Kr IV] 4p^3 ^{2}D$^o_{5/2}$–4p^3 ^{2}P$^o_{3/2}$ λ6798.4	6798.01?	-17.2	2/0	8 bl	6798.15	-11.0	2/0	7D	···	···	···	···	6798.36	-1.8	3/1	4Abl	···	···	···	···		
C II 3s′ ^{4}P$^o_{3/2}$–3p′ ^{4}D$_{1/2}$ (V14) λ6798.10	2.8(-5)	-4.0	7/2	1Abl	1.4(-5)	2.2	7/5	1A*	[8.1(-6)]	···	···	···	4.1(-5)	11.5	7/1	7 bl	[2.1(-5)]	···	···	···	B95	
Ca I 3d5s ^{1}D$_2$–3d13p ^{1}P$^o_1$ λ6798.28	*1.3(-5)*	-11.9	0/0	6		-5.7	···	···		···	···	···	*1.6(-5)*	3.5	0/0	5B		···	···	···		
[Kr V] 4p^2 ^{3}P$_1$–4p^2 ^{1}D$_2$ λ6256.06	6256.31	12.0	0/0	5Dbl	6256.57	24.5	0/0	7 bl	6256.31	12.0	0/0	5D	6256.38	15.3	1/0	7 bl	···	···	···	···		
C II 4p ^{2}P$^o_{1/2}$–5d ^{2}D$_{3/2}$ (V10.03) λ6257.18	4.4(-5)	-41.7	2/0	8	5.2(-5)	-29.2	2/0	8	1.5(-5)	-41.7	2/0	8	1.7(-4)	-38.4	···	··bl	[8.4(-5)]	···	···	···	S03	
C II 3d′ ^{2}D$^o_{3/2}$– 4p′ ^{2}P$_{1/2}$ (V38.03) λ6256.52	*1.5(-5)*	-10.1	2/0	5D	*8.0(-6)*	2.4	2/1	2Abl		-10.1	2/0	5D*	*1.2(-4)*	-6.7	2/0	6 bl		···	···	···	Z05	
S II 5p ^{4}S$^o_{3/2}$–7s ^{4}P$_{5/2}$ λ6256.35		-1.9	1/0	4A		10.5	1/0	6		-1.9	1/0	4A		1.4	1/0	5D		···	···	···		
Fe I a3H$_4$–z3G$^o_4$ (V169) λ6256.36		-2.4	5/0	4A		10.1	5/0	5D		-2.4	5/0	4A		1.0	5/0	4A		···	···	···		
O I 3p′ ^{3}F$_4$–4d′ ^{3}G $^o_3$ (V50) λ6256.47		-7.7	4/0	4A		4.8	4/0	5D		-7.7	4/0	5D		-4.3	4/0	5D		···	···	···		
C II 4p′ ^{4}D$_{5/2}$–5d′ ^{4}D$^o_{7/2}$ λ6256.24		3.4	4/0	5D		15.8	4/0	7		3.4	4/0	4A		6.7	4/0	7		···	···	···		
Ca I 4s9s ^{1}S$_0$–3d25p ^{1}P$^o_1$ λ6256.45		-6.7	0/0	5D		5.8	···	···		-6.7	0/0	5D		-3.3	0/0	4A		···	···	···		
[Co II] a3D$_2$–a1F$_3$ λ6256.46		-7.2	1/0	5D		5.3	1/0	4B		-7.2	1/0	5D		-3.8	1/0	4A		···	···	···		
SKY: OH 9-3 Q$_2$(0.5) λ6256.94		···	···	···		5.3	···	··bl		···	···	···		-34.0	···	··bl		···	···	···		
SKY: OH 9-3 Q$_1$(1.5) λ6257.96		-12.4	···	··bl		···	···	···		···	···	···		···	···	···		···	···	···		
[Kr V] 4p^2 ^{3}P$_2$–4p^2 ^{1}D$_2$ λ8243.39	OUT	···	···	···	OUT	···	···	···	OUT	···	···	···	8244.33?	34.2	···	···:	8243.70	11.3	···	···		h
N I 3s ^{4}P$_{5/2}$–3p ^{4}P$^o_{3/2}$ (V2) λ8242.39		···	···	···		···	···	···		···	···	···	1.4(-4)	70.9	···	···	4.2(-4)	47.7	···	···	B95	
H I 3–43 λ8243.69		···	···	···		···	···	···		···	···	···		23.3	0/0	5A		0.4	0/0	2A*	S03	

Table 7—Continued

Transition	NGC 2440 λ_o, I/I$_{H\beta}$[a]	NGC 2440 δV[b] (km s^{-1})	NGC 2440 Mult[c]	NGC 2440 IDI[d]	IC 2501 λ_o, I/I$_{H\beta}$	IC 2501 δV (km s^{-1})	IC 2501 Mult	IC 2501 IDI	IC 4191 λ_o, I/I$_{H\beta}$	IC 4191 δV (km s^{-1})	IC 4191 Mult	IC 4191 IDI	NGC 7027 λ_o, I/I$_{H\beta}$	NGC 7027 δV (km s^{-1})	NGC 7027 Mult	NGC 7027 IDI	IC 418 λ_o, I/I$_{H\beta}$	IC 418 δV (km s^{-1})	IC 418 Mult	IC 418 IDI	Ref Notes
O III 5g G ^{2}[9/2]^o–6h H ^{2}[11/2] λ8244.10	...	...	...		...	...	...		...	...	...		8.4		0/0	7B	-14.6	...	...		B95

References. — B95=PN NGC 7027 (Baluteau et al. 1995), B00=Orion Nebula (Baldwin et al. 2000), E04=Orion Nebula (Esteban et al. 2004), H95=PN NGC 6886 (Hyung et al. 1995), H01=PN IC 5217 (Hyung et al. 2001), P04=PN NGC 5315 (Peimbert et al. 2004), S03=PN IC 418 (Sharpee et al. 2003), ZL02=PN Mz 3 (Zhang & Liu 2002), and Z05=PN NGC 7027 (Zhang et al. 2005)

[a]Wavelength: 1) λ_o are geocentric corrected wavelength in Å, 2) "OUT" means not in observed range, 3) "?" denotes an uncertain feature. Intensity: 1) numbers in parentheses are exponents, 2) italics denote corrected intensities attributable to the *s*-process transition, 3) bracketed values as upper limits for unobserved features.

[b]Observed (λ_o)-transition wavelength (km s^{-1}).

[c]EMILI multiplet check statistics: number expected/number observed

[d]EMILI IDI value/rank followed by asterisk (certain ID), colon (uncertain ID), or "bl" (blend). Definition of IDI given in Section 6

[e]Unidentified line in IC 418 Baldwin et al. (2000).

[f]Unidentified line in Orion Nebula Sharpee et al. (2003).

[g]NGC 2440, IC 4191, NGC 7027: Identified as a separate line.

[h]NGC 7027: Affected strongly by telluric absorption.

Table 8. Possible Xenon Line Identifications

Transition	NGC 2440				IC 2501				IC 4191				NGC 7027				IC 418				Ref	Notes
	λ_o, I/I$_{H\beta}$[a]	δV[b] (km s^{-1})	Mult[c]	IDI[d]	λ_o, I/I$_{H\beta}$	δV (km s^{-1})	Mult	IDI	λ_o, I/I$_{H\beta}$	δV (km s^{-1})	Mult	IDI	λ_o, I/I$_{H\beta}$	δV (km s^{-1})	Mult	IDI	λ_o, I/I$_{H\beta}$	δV (km s^{-1})	Mult	IDI		
[Xe III] 5p^4 ^{3}P$_2$–5p^4 ^{1}D$_2$ λ5846.77	5846.73	-2.1	···	···	5846.64?	-6.7	···	···:	5846.77	0.0	···	···	5846.65	-6.2	···	··bl	5846.70	-3.6	0/0	5 *		e
He II 5–31 λ5846.66	3.2(-4)	3.6	0/0	5B*	7.7(-6)	-1.0	0/0	3A	5.2(-5)	5.6	0/0	4A*	4.2(-4)	-0.5	0/0	1Abl	1.3(-4)	2.1	0/0	3A	Z05	
[Fe II] a2G$_{7/2}$–c2G$_{9/2}$ λ5847.32		-30.3	3/0	7C		-34.9	3/0	7C		-28.2	3/0	7C	*1.4(-4)*	-34.4	3/0	···		-31.8	3/0	···		
Fe II 4d e4F$_{5/2}$–4f 2[3]$^o_{5/2}$ λ5846.78		-2.6	0/0	3A		-7.2	0/0	4B		-0.5	0/0	4A		-6.7	0/0	4B		-4.1	0/0	4C		
Fe I x5P$^o_1$–6d 2[3/2]$_1$ λ5846.60		6.7	···	···		2.1	···	···		8.7	···	···		2.6	···	···		5.1	0/0	3A		
[Xe IV] 5p^3 ^{4}S$^o_{3/2}$–5p^3 ^{2}D$^o_{5/2}$ λ5709.20	5708.95?	-13.1	0/0	5 *	5708.97?	-12.1	1/0	5 :	5708.98?	-11.6	1/0	7 *	5708.89	-16.2	1/1	7 *	5708.91?	-15.2	1/1	7 *		e
N II 3s ^{3}P$^o_2$–3p ^{3}D$_2$ (V3) λ5710.77	1.2(-5)	-95.6	···	···	6.5(-6)	-94.6	···	···	1.2(-5)	-94.1	···	···	1.1(-4)	-98.8	···	···	1.9(-5)	-97.7	···	···	many	f
[Fe I] a5D$_3$–a5P$_1$ λ5708.97		-1.1	7/0	4C		0.0	7/1	3A:		0.5	7/0	4B		-4.2	7/0	5C		-3.2	7/0	5B		
Si I 4p ^{3}D$_2$–18s (3/2,1/2)$^o_1$ λ5708.91		2.1	0/0	3A		3.2	0/0	3A		3.7	0/0	3A		-1.1	0/0	3A		0.0	0/0	4A		
Fe II] y4P$^o_{3/2}$–e6D$_{1/2}$ λ5709.04		-4.7	7/1	3A		-3.7	7/0	5		-3.2	7/0	5D		-7.9	7/1	6D		-6.8	7/0	8		
[Xe IV] 5p^3 ^{4}S$^o_{3/2}$–5p^3 ^{2}D$^o_{3/2}$ λ7535.4	7534.70	-27.9	0/0	7 *	7534.71	-27.5	···	···*	7534.73	-26.7	1/0	8 *	7534.94	-18.3	1/1	6 *	7534.90	-19.9	1/1	6 *		g
Fe II] b2F$_{5/2}$–z4F$^o_{5/2}$ (V87) λ7534.82	1.3(-5)	-4.8	0/0	2A	1.6(-5)	-4.4	1/0	4A	3.6(-5)	-3.6	1/0	3B	1.7(-4)	4.8	5/0	6	1.6(-5)	3.2	5/0	4A	H01	h
N II 5f.G 2[7/2]$_4$–10d ^{1}F$^o_3$ λ7535.10		-15.9	0/0	6		-15.5	0/0	6C		-14.7	0/0	5		-6.4	0/0	3A		-8.0	0/0	5	E04,P04	
Ne I 3p 2[1/2]$_1$–3d 2[1/2]$^o_1$ (V8.01) λ7535.77		-42.6	0/0	7		-42.2	···	···		-41.4	···	···		-33.0	···	···		-34.6	···	···		
[Cr II] b4D$_{5/2}$–c4D$_{5/2}$ λ7534.80		-4.0	4/0	5		-3.6	8/0	6C		-2.8	8/0	4C		5.6	8/0	6		4.0	8/0	4A		
Ne II 3d′ ^{2}P$_{3/2}$–6f 2[3]$^o_{5/2}$ λ7534.75		-2.0	0/0	3B		-1.6	0/0	5B		-0.8	0/0	2A		7.6	0/0	5D		6.0	0/0	4A		
[Xe V] 5p^2 ^{3}P$_0$–5p^2 ^{3}P$_2$ λ7076.8	7077.02	9.3	···	···	···	···	···	···	7076.94?	5.9	0/0	4A*	7077.00	8.5	0/0	6 :	···	···	···	···		
C I 3p ^{3}D$_2$–4d ^{3}D$^o_2$ (V26.01) λ7076.48	1.5(-5)	22.9	···	···	[5.5(-5)]	···	···	···	3.9(-6)	19.5	6/0	8	2.0(-5)	22.0	6/0	8	[2.8(-5)]	···	···	···	B95	
[Fe III] 3d^6 ^{3}P4$_1$–3d^6 ^{1}S4$_0$ λ7078.10		-45.8	0/0	5A		···	···	···		-49.2	0/0	···		-46.6	0/0	···		···	···	···	ZL02	
[Ni II] 4s ^{4}F$_{3/2}$–4s ^{4}P$_{3/2}$ λ7078.04		-20.3	···	···		···	···	···		-46.6	···	···		-44.1	···	···		···	···	···	ZL02	
Ni II 5d ^{4}F$_{7/2}$–4f 2[3]$^o_{7/2}$ λ7076.90		28.0	···	···		···	···	···		1.7	0/0	4A		4.2	0/0	5C		···	···	···		
Ca I 4s15s ^{3}S$_1$–3d22p ^{3}P$^o_1$ λ7077.02		22.9	···	···		···	···	···		-3.4	0/0	5C		-0.8	0/0	4A		···	···	···		
Ca I 4s14s ^{1}S$_0$–3d17f ^{1}P$^o_1$ λ7077.08		20.8	···	···		···	···	···		-5.5	0/0	5C		-3.0	0/0	4A		···	···	···		
SKY: 3-2 O$_2$ $b\,^1\Sigma^+_g$–$X\,^3\Sigma^-_g$ P$_{12}$(11) λ7078.58		0.4	···	···*		···	···	···		···	···	···		···	···	···		···	···	···		
[Xe VI] 5p ^{2}P$^o_{1/2}$–5p ^{2}P$^o_{3/2}$ λ6408.9	6408.69?	-9.8	···	···:	···	···	···	···	6408.96?	2.8	···	···:	6408.61	-13.6	···	···*	···	···	···	···		
He II 5–15 λ6406.38	2.8(-5)	108.1	···	···	[2.4(-6)]	···	···	···	1.6(-6)	120.8	···	···	2.0(-4)	104.4	···	···	[9.3(-6)]	···	···	···		i
[Fe III] 3d^6 ^{1}S4$_0$–3d^6 ^{3}P2$_2$ λ6408.50		8.9	1/0	4A		···	···	···		21.5	1/0	6A		5.1	1/0	4A		···	···	···		
C IV 9–17 λ6408.70		-0.5	···	···		···	···	···		12.2	···	···		-4.2	0/0	5B		···	···	···		

References. — E04=Orion Nebula (Esteban et al. 2004), H01=PN IC 5217 (Hyung et al. 2001), P04=PN NGC 5315 (Peimbert et al. 2004), ZL02=PN Mz 3 (Zhang & Liu 2002), and Z05=PN NGC 7027 (Zhang et al. 2005)

[a−d]Same as for Table 7.

[e]Unidentified line in IC 418 (Sharpee et al. 2003).

[f]Identified as separate line in all spectra.

[g]On edge of NGC 2440, IC 2501, IC 4191 spectra, where poorest wavelength calibration is expected.

[h]Listed by Hyung et al. (2001) as "unlikely ID".

[i]IC 4191 and NGC 7027: Identified as separate line.

Table 9. Possible Bromine Line Identifications

Transition	NGC 2440				IC 2501				IC 4191				NGC 7027				IC 418				Ref	Notes
	λ_o, I/I$_{H\beta}$[a]	δV[b] (km s^{-1})	Mult	IDI[c]	λ_o, I/I$_{H\beta}$	δV (km s^{-1})	Mult	IDI	λ_o, I/I$_{H\beta}$	δV (km s^{-1})	Mult	IDI	λ_o, I/I$_{H\beta}$	δV (km s^{-1})	Mult	IDI	λ_o, I/I$_{H\beta}$	δV (km s^{-1})	Mult	IDI		
[Br III] 4p^3 ^{4}S$^o_{3/2}$–4p^3 ^{2}D$^o_{5/2}$ λ6131.0	...	...	...	...	6130.70	-14.7	1/1	4A*	6130.34	-32.3	1/1	6 *	6130.32	-33.3	...	..bl	6130.47	-25.9	...	..*		e,f
C III 7h ^{1,3}H^o–16g ^{1,3}G λ6130.30	[1.7(-5)]	...	...	...	1.7(-5)	19.6	0/0	5B	3.8(-5)	2.0	0/0	2A	1.1(-4)	1.0	0/0	2Abl	2.8(-5)	8.3	0/0	2A		
]Ni VI] 3d^5 ^{4}D$_{5/2}$–3d^5 ^{2}F1$_{7/2}$ λ6130.40		...	...	...		14.7	1/0	7		-2.9	1/0	5D	*7.7(-5)*	-3.9	1/0	4C		3.4	1/0	4C		
[Br III] 4p^3 ^{4}S$^o_{3/2}$–4p^3 ^{2}D$^o_{3/2}$ λ6556.4	6555.98?	-19.2	1/0	7 :	6555.92?	-22.0	1/1	6 *	6555.87?	-24.2	1/1	6 *	6555.93?	-21.5	1/0	8 *	...	...	...	...		e
Fe II 4d ^{4}P$_{3/2}$–4f ^{2}[2]$^o_{5/2}$ λ6555.94	4.2(-5)	1.8	0/0	3	7.3(-5)	-0.9	0/0	2A	8.5(-5)	-3.2	0/0	2A	4.3(-4)	-0.5	0/0	2A	[2.1(-4)]	...	...	...		
O II 4f F ^{2}[4]$^o_{9/2}$–6g ^{2}[5]$_{11/2}$ λ6555.84		6.4	0/0	3		3.7	0/0	2A		1.4	0/0	2A		4.1	0/0	3B		...	...	...		
N II 4f F ^{2}[5/2]$_3$–6d ^{3}D$^o_2$ λ6556.06		-3.7	0/0	2A		-6.4	0/0	2A		-8.7	0/0	3C		-5.9	0/0	3B		...	...	...		
O II 4f F ^{2}[4]$^o_{9/2}$–6g ^{2}[5]$_{9/2}$ λ6555.99		-0.5	0/0	2A		-3.2	0/0	3D		-5.5	0/0	3C		-2.7	0/0	3B		...	...	...		
O II 4f′ H ^{2}[5]$^o_{9/2,11/2}$–6g′ ^{2}[6] λλ6556.05,.08		-3.2	0/0	2A		-5.9	0/0	3D		-8.2	0/0	3C		-5.5	0/0	4		...	...	...		
O II 4f F ^{2}[4]$^o_{9/2}$–6g ^{2}[4]$_{9/2}$ λ6556.10		-5.5	0/0	2A		-8.2	0/0	4		-10.5	0/0	4		-7.8	0/0	5		...	...	...		
[Br IV] 4p^2 ^{3}P$_1$–4p^2 ^{1}D$_2$ λ7368.1	...	...	...	...	...	...	...	...	...	...	...	...	7367.62?	-19.5	1/0	9 :	...	...	...	...		
C II 3p′ ^{2}D$_{5/2}$–3d′ ^{2}P$^o_{3/2}$ λ7370.00	[2.6(-5)]	...	...	...	[4.4(-5)]	...	...	...	[3.5(-5)]	...	...	...	4.4(-5)	-96.9	...	...	[4.9(-5)]	...	...	...	B95	
O II 4p ^{2}S$^o_{1/2}$–5s ^{2}P$_{3/2}$ λ7367.68		...	...	...		...	...	...		...	...	...		-2.4	1/0	3A		...	...	...		
C V 7p ^{3}P^o–8d ^{3}D 7367.60		...	...	...		...	...	...		...	...	...		0.8	0/0	4B		...	...	...		
[Br IV] 4p^2 ^{3}P$_2$–4p^2 ^{1}D$_2$ λ9450.5	OUT	...	...	...	OUT	...	...	...	OUT	...	...	...	9450.85?	11.1	1/0	8 :	...	...	...	...		
Fe I v3D$^o_2$–6d 2[5/2]$_3$ λ9450.95		...	...	...		...	...	...		...	...	...	7.5(-5)	-3.2	0/0	3A	[5.3(-5)]	...	...	...		

References. — B95=PN NGC 7027 (Baluteau et al. 1995)

[a−d]Same as for Table 7.

[e]Computed using energy levels from Biémont & Hansen (1986a), see text.

[f]Unidentified line in IC 418 Sharpee et al. (2003).

Table 10. Possible Identifications From Other Z> 30 Ions

Transition	NGC 2440				IC 2501				IC 4191				NGC 7027				IC 418				Ref	Notes
	λ_o, I/I$_{H\beta}$[a]	δV[b] (km s^{-1})	Mult[c]	IDI[d]	λ_o, I/I$_{H\beta}$	δV (km s^{-1})	Mult	IDI	λ_o, I/I$_{H\beta}$	δV (km s^{-1})	Mult	IDI	λ_o, I/I$_{H\beta}$	δV (km s^{-1})	Mult	IDI	λ_o, I/I$_{H\beta}$	δV (km s^{-1})	Mult	IDI		
[Rb IV] 4p^4 ^{3}P$_2$–4p^4 ^{1}D$_2$ λ5759.55	5759.98	22.4	···	···	···	···	···	···	5759.61	3.1	···	··bl	5759.59	2.1	···	··bl	5759.78?	12.0	···	···:		e,*f*
He II 5–47 λ5759.74	5.1(-4)	12.5	0/0	6B*	[2.5(-6)]	···	···	···	2.4(-5)	-6.8	0/0	4Bbl	3.1(-4)	-7.8	0/0	5Abl	2.0(-5)	2.1	0/0	3A	Z05	
[Fe II] a2H$_{9/2}$–c2D$_{5/2}$ λ5759.30		35.4	0/0	5A		···	···	···	*1.5(-5)*	16.1	0/0	3A	*2.0(-4)*	15.1	0/0	6B		25.0	0/0	5B		
[Rb V] 4p^3 ^{4}S$^o_{3/2}$–4p^3 ^{2}D$^o_{3/2}$ λ5363.6	···	···	···	···	5363.81	11.7	···	···:	5363.96?	20.1	···	···:	5363.62	1.1	···	···*	···	···	···	···		
[Ni IV] 3d′ ^{4}F$_{7/2}$–3d′ ^{2}G$_{9/2}$ λ5363.35	[3.4(-5)]	···	···	···	6.7(-6)	25.7	4/0	7	5.4(-6)	34.1	4/0	8C	9.0(-5)	15.1	4/0	7B	[2.3(-5)]	···	···	···	many	
O II 4f.F ^{2}[4]$^o_{7/2}$–4d′ ^{2}F$_{7/2}$ λ5363.80		···	···	···		0.6	0/0	3A		8.9	0/0	5A		-10.1	0/0	6A		···	···	···		
[Cr II] a4D$_{3/2}$–c4D$_{7/2}$ λ5363.77		···	···	···		2.2	6/1	4B		10.6	6/0	7B		-8.4	6/0	8C		···	···	···		
[Te III] 5p^2 ^{3}P$_1$–5p^2 ^{1}D$_2$ λ7933.3	OUT	···	···	···	OUT	···	···	···	OUT	···	···	···	···	···	···	···	7932.98	-12.1	···	··*		e
He I 3p ^{3}P^o–28s ^{3}S λλ7932.36,.41		···	···	···		···	···	···		···	···	···	[2.0(-5)]	···	···	···	1.7(-5)	21.6	0/0	6A		
[I III] 5p^2 ^{4}S$^o_{3/2}$–5p^2 ^{2}D$^o_{3/2}$ λ8536.5	OUT	···	···	···	OUT	···	···	···	OUT	···	···	···	8536.66?	5.6	1/0	6B:	···	···	···	···		
Cr II 5p ^{6}D$^o_{3/2}$–6s ^{6}D$_{5/2}$ λ8536.68		···	···	···		···	···	···		···	···	···	1.7(-5)	-0.7	9/1	4A	[2.3(-5)]	···	···	···		
Ba II 5d ^{2}D$_{5/2}$–6p ^{2}P$^o_{3/2}$ λ6141.71	6141.61	-4.9	···	···:	···	···	···	···	6141.59	-5.9	···	···*	6141.51	-9.8	···	···:	···	···	···	···		
O I 18d ^{3}D$^o_2$–4p′ ^{3}D$_3$ λ6141.75	8.4(-5)	-6.8	4/0	5A	[4.0(-6)]	···	···	···	2.7(-5)	-7.8	4/0	6A	7.3(-5)	-11.7	4/0	8	[1.8(-5)]	···	···	···		
Ne III 4p ^{5}P$_3$–4d ^{5}D$^o_4$ λ6141.48		6.4	···	···		···	···	···		5.4	···	···		1.5	2/1	2A:		···	···	···		
[Ni III] 4s ^{3}F$_2$–4s ^{3}P$_1$ λ6141.83		-10.7	5/1	5A:		···	···	···		-11.7	5/0	7B		-15.6	5/0	8		···	···	···		
[Ba IV] 5p^5 ^{2}P$^o_{3/2}$–5p^5 ^{2}P$^o_{1/2}$ λ5696.6	···	···	···	···	···	···	···	···	···	···	···	···	5696.19	-21.6	0/0	8 bl	···	···	···	···		
C III 2s ^{1}P$^o_1$–3d ^{1}D$_2$ (V2) λ5695.92	[2.1(-5)]	···	···	···	[2.5(-6)]	···	···	···	[6.2(-6)]	···	···	···	5.9(-5)	14.2	0/0	6Cbl	[1.5(-5)]	···	···	···	Z05	
S II 4d′ ^{2}G$_{7/2}$–5f′ 2[5]^o λ5696.14		···	···	···		···	···	···		···	···	···	*2.1(-5)*	2.6	0/0	4A		···	···	···		
[Pb II] 6p ^{2}P$^o_{1/2}$–6p ^{2}P$^o_{3/2}$ λ7099.8	···	···	···	···	···	···	···	···	···	···	···	···	7099.78	-0.8	···	···*	7099.93	5.5	0/0	4A*		e
Si I 4p ^{1}S$_0$–18d (3/2,5/2)$^o_1$ λ7099.70	[2.4(-5)]	···	···	···	[4.5(-6)]	···	···	···	[6.9(-6)]	···	···	···	4.6(-5)	3.4	0/0	3A	2.4(-5)	9.7	0/0	4A		
Ar I 3d 2[1/2]$^o_0$–9f 2[3/2] λ7099.82		···	···	···		···	···	···		···	···	···		-1.7	0/0	4B		4.6	0/0	4A		
Ca I 4s16d ^{3}D–3d51p ^{3}D^o λ7099.82		···	···	···		···	···	···		···	···	···		-1.7	0/0	4B		4.6	0/0	4A		
Ca I 4s17d ^{1}D$_2$–3d47p ^{1}P$^o_1$ λ7099.78		···	···	···		···	···	···		···	···	···		0.0	0/0	4B		6.3	0/0	4A		

References. — Z05=PN NGC7027 (Zhang et al. 2005)

[a−d]Same as for Table 7.

[e]Unidentified line in IC 418 Sharpee et al. (2003).

[f]NGC 2440, IC 4191: Contaminated by flare or ghost.

Table 11. Summary of Possible Z>30 Ion Line Intensities[a]

	PNe							H II regions	
				NGC 7027					
Transition	NGC 2440	IC 2501	IC 4191	(a)	(b)	(c)	IC 418	Orion	NGC 3576
[Br III] λ6131.0	<1.7(-5)	**1.7(-5)**	**3.8(-5)**	**7.7(-5)**	**7.6(-5)**	<1.1(-4)	**2.8(-5)**	···	···
[Br III] λ6556.4	4.2(-5)	**7.3(-5)**	**8.5(-5)**	**4.3(-4)**	···	···	···	···	···
[Br IV] λ7368.1	<2.6(-5)	<4.4(-5)	<3.5(-5)	4.4(-5)	2.0(-5)	···	<4.9(-5)	···	···
[Br IV] λ9450.5	···	···	···	7.5(-5)	<7(-6)	···	<5.3(-5)	···	···
[Kr III] λ6826.70	···	**2.5(-5)**	1.5(-5)	**4.6(-4)**	**4.1(-4)**	4.4(-4)	**3.2(-4)**	7.0(-5)	<3.0(-5)
[Kr IV] λ5346.02	**3.5(-4)**	**6.1(-5)**	**2.4(-4)**	**1.9(-3)**	**1.9(-3)**	1.5(-3)	**3.5(-5)**	···	···
[Kr IV] λ5867.74	**4.6(-4)**	**8.5(-5)**	**1.9(-4)**	**2.6(-3)**	**2.6(-3)**	2.3(-3)	**3.5(-5)**	7.8(-5)	<5.0(-5)
[Kr IV] λ6107.8	5.6(-6)	<4.3(-6)	···	**7.2(-5)**	**6.3(-5)**	5(-5)	<1.4(-5)	···	···
[Kr IV] λ6798.4	**1.3(-5)**	···	<8.1(-6)	**1.6(-5)**	2(-5)	···	<2.1(-5)	···	···
[Kr V] λ6256.06	**1.5(-5)**	**8.0(-6)**	···	**1.2(-4)**	**1.5(-4)**	1.8(-4)	<8.4(-5)	···	···
[Kr V] λ8243.39	···	···	···	1.4(-4)	**2.0(-4)**	···	···	···	···
[Rb IV] λ5759.55	···	<2.5(-6)	**1.5(-5)**	**2.0(-4)**	**1.7(-4)**	2.3(-4)	2.0(-5)	···	···
[Rb V] λ5363.6	<3.4(-5)	6.7(-6)	5.4(-6)	**9.0(-5)**	8.3(-5)	···	<2.3(-5)	5.6(-6)	···
[Te III] λ7933.3	···	···	···	<2.0(-5)	<1.1(-5)	···	**1.7(-5)**	···	···
[I III] λ8536.5	···	···	···	1.7(-5)	2.3(-5)	···	<2.3(-5)	···	···
[Xe III] λ5846.77	···	7.7(-6)	···	**1.4(-4)**	**5.3(-5)**	1.2(-4)	**1.3(-4)**	<7.8(-5)	···
[Xe IV] λ5709.2	**1.2(-5)**	6.5(-6)	**1.2(-5)**	**1.1(-4)**	**1.1(-4)**	9(-5)	**1.9(-5)**	<7.8(-5)	<5.0(-5)
[Xe IV] λ7535.4	**1.3(-5)**	**1.6(-5)**	**3.6(-5)**	**1.7(-4)**	**1.9(-6)**	1.4(-4)	**1.6(-5)**	···	<2.0(-5)
[Xe V] λ7076.8	···	<5.5(-5)	**3.9(-6)**	2.0(-5)	···	···	<2.8(-5)	···	···
[Xe VI] λ6408.9	2.8(-5)	<2.4(-6)	1.6(-6)	**2.0(-4)**	**1.3(-4)**	···	<9.3(-6)	···	···
Ba II λ6141.71	8.4(-5)	<4.0(-6)	**2.7(-5)**	7.3(-5)	**7.5(-5)**	7(-5)	<1.8(-5)	···	···
[Ba IV] λ5696.6	<2.1(-5)	<2.5(-6)	<6.2(-6)	**2.1(-5)**	**7.3(-5)**	8(-5)	<1.5(-5)	···	···
[Pb II] λ7099.8	<2.4(-5)	<4.5(-6)	<6.9(-6)	**4.6(-5)**	**3.5(-5)**	1.0(-4)	**2.4(-5)**	···	···

References. — NGC 7027=(a) present measurement; (b) Péquignot & Baluteau (1994); (c) Zhang et al. (2005); Orion=Baldwin et al. (2000); NGC 3576=García-Rojas et al. (2004)

[a]In units of I(Hβ)=1, certain identifications in bold.

Table 12. *s*-process Ionic/Elemental Abundances[a]

	PNe					H II regions	
X^{+i}/H$^+$/Transition	NGC 2440	IC 2501	IC 4191	NGC 7027	IC 418	Orion	NGC 3576
Br^{+2}/H^+ λ6131.0	<1.77	$2.21^{+0.16}_{-0.19}$	$2.18^{+0.14}_{-0.17}$	$2.52^{+0.09}_{-0.10}$	$2.41^{+0.17}_{-0.22}$	···	···
Br^{+2}/H^+ λ6556.4	$2.13^{+0.19}_{-0.28}$	$2.70^{+0.18}_{-0.22}$	$2.44^{+0.16}_{-0.21}$	$3.14^{+0.10}_{-0.12}$	<3.07	···	···
Adopted	$2.13^{+0.19}_{-0.28}$	$2.27^{+0.14}_{-0.15}$	$2.24^{+0.11}_{-0.13}$	$2.57^{+0.08}_{-0.09}$	$2.41^{+0.17}_{-0.22}$	···	···
Br^{+3}/H^+ λ7368.1	<2.21	<2.89	<2.74	$2.53^{+0.09}_{-0.11}$	<3.00	···	···
Br^{+3}/H^+ λ9450.5	···	···	···	$2.74^{+0.11}_{-0.14}$	<3.02	···	···
..... Adopted	<2.21	<2.89	<2.74	$2.58^{+0.08}_{-0.09}$	<3.00	···	···
Kr^{+2}/H^+ λ6826.70	···	$2.4^{+0.3}_{-0.5}$	$1.89^{+0.13}_{-0.17}$	$3.39^{+0.07}_{-0.08}$	$3.53^{+0.13}_{-0.16}$	3.01	<2.47
Kr^{+3}/H^+ λ5346.02	$2.96^{+0.09}_{-0.10}$	$2.75^{+0.12}_{-0.15}$	3.28±0.10	$3.78^{+0.02}_{-0.03}$	$2.60^{+0.17}_{-0.18}$	···	···
..... λ5867.74	$2.96^{+0.09}_{-0.10}$	$2.69^{+0.12}_{-0.15}$	2.99±0.10	3.77±0.02	$2.40^{+0.16}_{-0.18}$	2.83	<2.60
..... λ6107.8	$2.8^{+0.2}_{-0.3}$	<3.44	···	$3.99^{+0.05}_{-0.06}$	<4.07	···	···
..... λ6798.4	$3.6^{+0.3}_{-0.7}$	···	<4.03	$3.8^{+0.3}_{-0.6}$	<4.65	···	···
..... Adopted	2.94±0.07	$2.72^{+0.09}_{-0.10}$	3.07±0.07	3.79±0.02	2.46±0.12	2.83	<2.60
Kr^{+4}/H^+ λ6256.06	$1.7^{+0.5}_{-1.7}$	$2.1^{+0.6}_{-2.1}$	···	3.00	<3.15	···	···
Kr^+4/H^+ λ8243.39	···	···	···	3.10	···	···	···
..... Adopted	$1.7^{+0.5}_{-1.7}$	$2.1^{+0.6}_{-2.1}$	···	$3.05^{+0.05}_{-0.06}$	<3.15	···	···
Xe^{+2}/H^+ λ5846.77	···	$1.3^{+0.2}_{-0.3}$	···	$2.2^{+0.2}_{-0.4}$	$2.53^{+0.13}_{-0.16}$	<2.47	···
Xe^{+3}/H^+ λ5709.2	$1.53^{+0.12}_{-0.15}$	$1.76^{+0.18}_{-0.28}$	$1.97^{+0.13}_{-0.15}$	2.58±0.04	$2.32^{+0.16}_{-0.18}$	<3.02	<2.80
..... λ7535.4	$1.46^{+0.12}_{-0.15}$	$1.94^{+0.12}_{-0.15}$	$2.25^{+0.12}_{-0.15}$	2.63±0.06	$2.02^{+0.16}_{-0.18}$	···	<2.15
..... Adopted	$1.49^{+0.09}_{-0.10}$	$1.87^{+0.11}_{-0.13}$	$2.05^{+0.10}_{-0.11}$	2.59±0.03	2.10±0.12	<3.02	<2.15
Xe^{+4}/H^+ λ7076.8	···	<3.01	$1.82^{+0.17}_{-0.27}$	$2.38^{+0.08}_{-0.09}$	<2.83	···	···
Xe^{+5}/H^+ λ6408.9	$1.17^{+0.16}_{-0.19}$	<0.68	$0.3^{+0.3}_{-0.4}$	2.28	<1.24	···	···
Ba^+/H^+ λ6141.71	$2.73^{+0.14}_{-0.16}$	<1.85	$2.5^{...}_{-0.2}$	$2.41^{...}_{-0.05}$	<1.97	···	···
Ba^{+3}/H^+ λ5696.6	<1.66	<1.15	<1.13	$1.7^{+0.3}_{-1.2}$	<1.90	···	···
Ar^{+2}/H^+	6.13±0.04	6.27±0.07	$5.70^{+0.05}_{-0.06}$	6.09±0.02	$6.01^{+0.06}_{-0.07}$	6.42	6.34±0.04[b]
Ar^{+2}/H^+	5.70±0.03	4.75±0.03	$5.74^{+0.03}_{-0.04}$	5.77±0.02	$2.96^{+0.12}_{-0.06}$	4.37	4.20±0.07[b]
Ar^{+4}/H^+	$5.24^{+0.06}_{-0.08}$	···	$4.57^{+0.09}_{-0.12}$	5.60	···	···	···
Br/Ar	···	···	···	$-3.22^{+0.16}_{-0.22}$	···	···	···
Kr/Ar	-3.33 ± 0.11	-3.3 ± 0.3	$-2.94^{+0.09}_{-0.10}$	-2.36 ± 0.04	$-2.44^{+0.14}_{-0.18}$	−3.19	< −3.50
Xe/Ar	$-4.64^{+0.12}_{-0.14}$	$-4.31^{+0.15}_{-0.19}$	$-3.78^{+0.13}_{-0.17}$	$-3.35^{+0.08}_{-0.09}$	$-3.34^{+0.14}_{-0.17}$	< −3.29	···
[Br/Ar]	···	···	···	$+0.73^{+0.16}_{-0.22}$	···	···	···
[Kr/Ar]	-0.07 ± 0.11	-0.1 ± 0.3	$+0.32^{+0.09}_{-0.10}$	$+0.90 \pm 0.04$	$+0.82^{+0.14}_{-0.18}$	+0.07	< −0.24
[Xe/Ar]	$-0.37^{+0.12}_{-0.14}$	$-0.04^{+0.15}_{-0.19}$	$+0.49^{+0.13}_{-0.17}$	$+0.92^{+0.08}_{-0.09}$	$+0.93^{+0.14}_{-0.17}$	< +0.98	···

[a]In units of 12+log(N/H).

[b]Ar abundances using $t^2 = 0.00$.

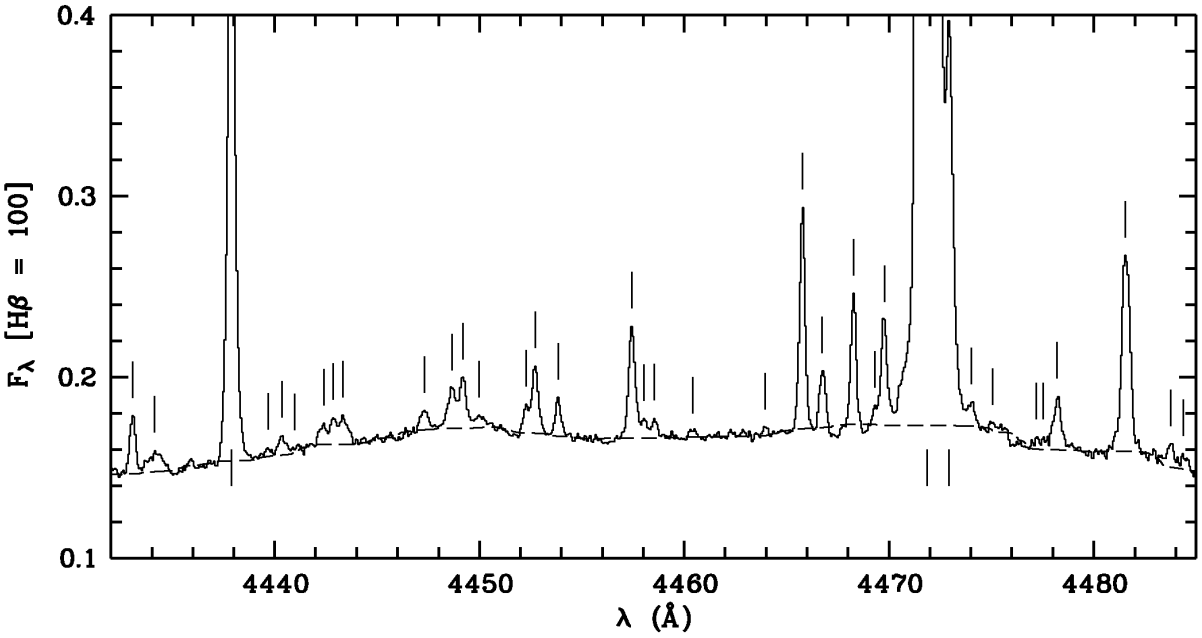

Fig. 1.— Portion of the IC 2501 spectrum illustrating the automated continuum fitting procedure. The vertical lines designate emission features defined by the ED fitting algorithm.

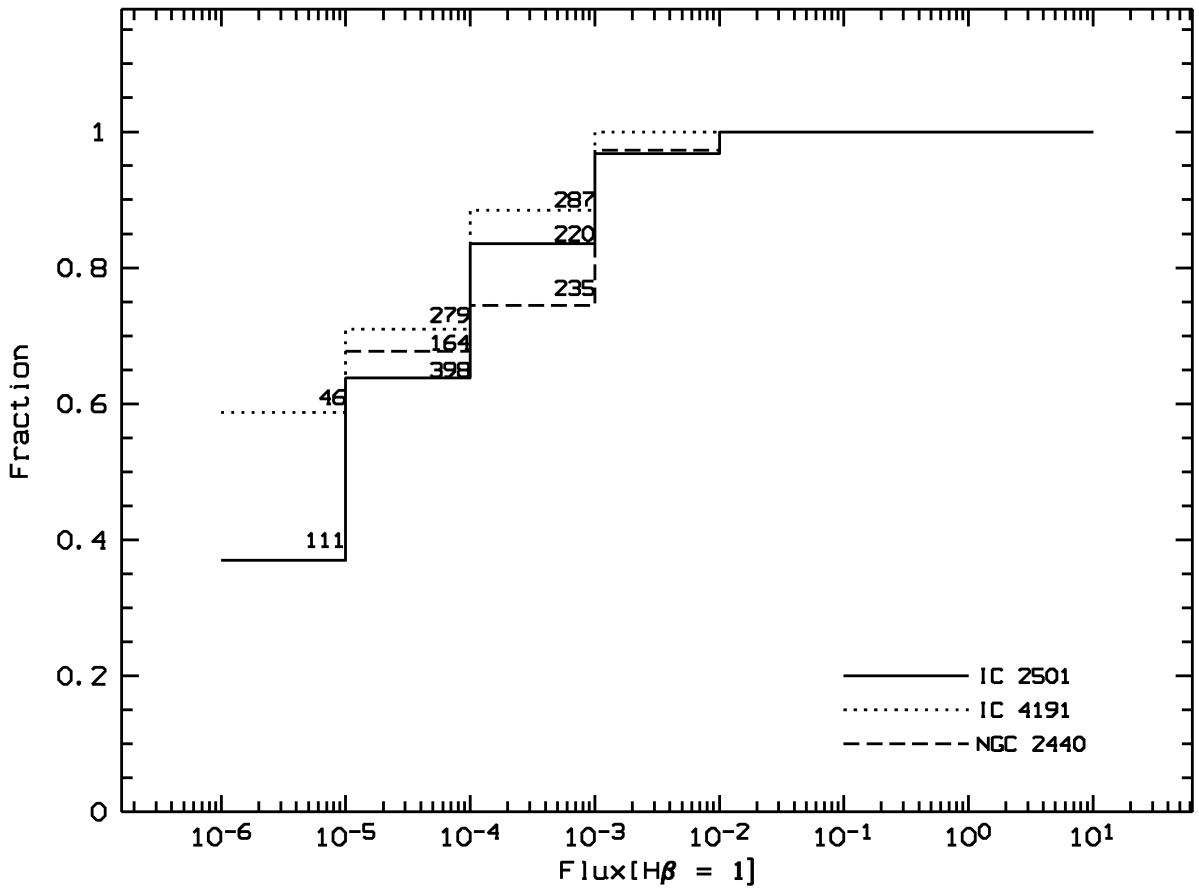

Fig. 2.— The fraction of lines present in the spectrum of each PN which are also detected in another of the PNe. The numbers give the total number of detected lines in each flux interval.

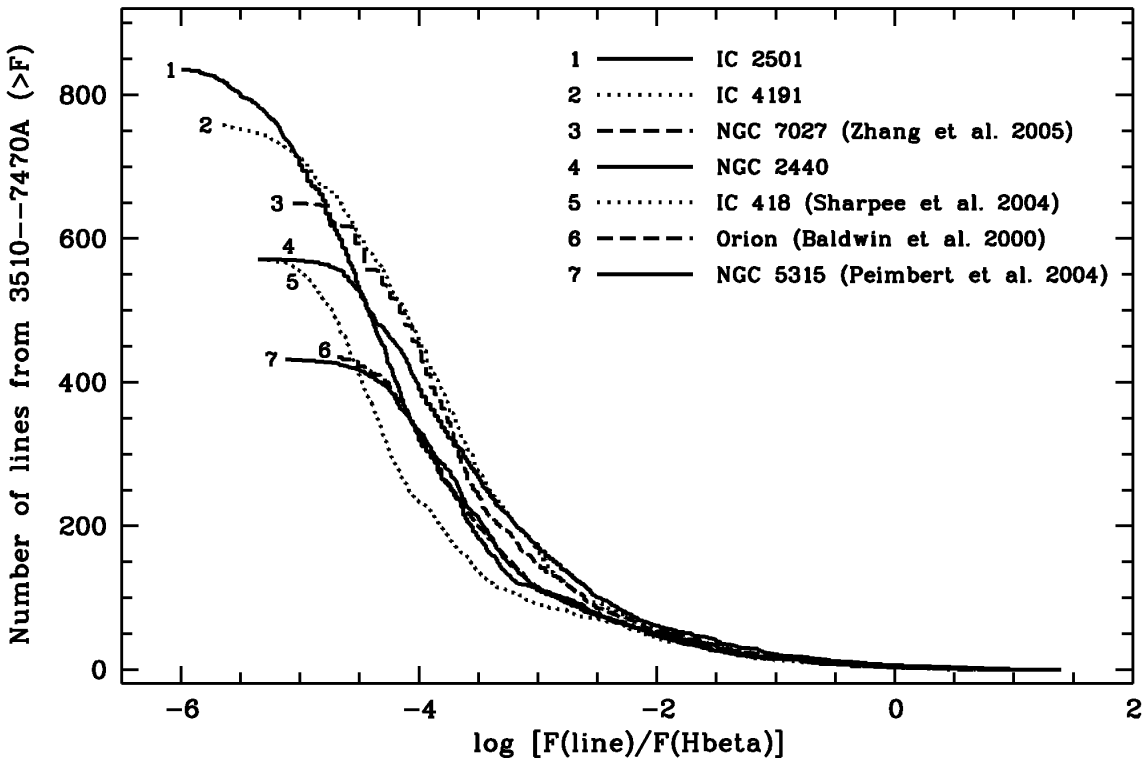

Fig. 3.— The cumulative number of observed lines exceeding a given flux level for recently published nebular spectra. We consider only those lines within the wavelength range 3510–7470 Å, which is covered by all the spectra.

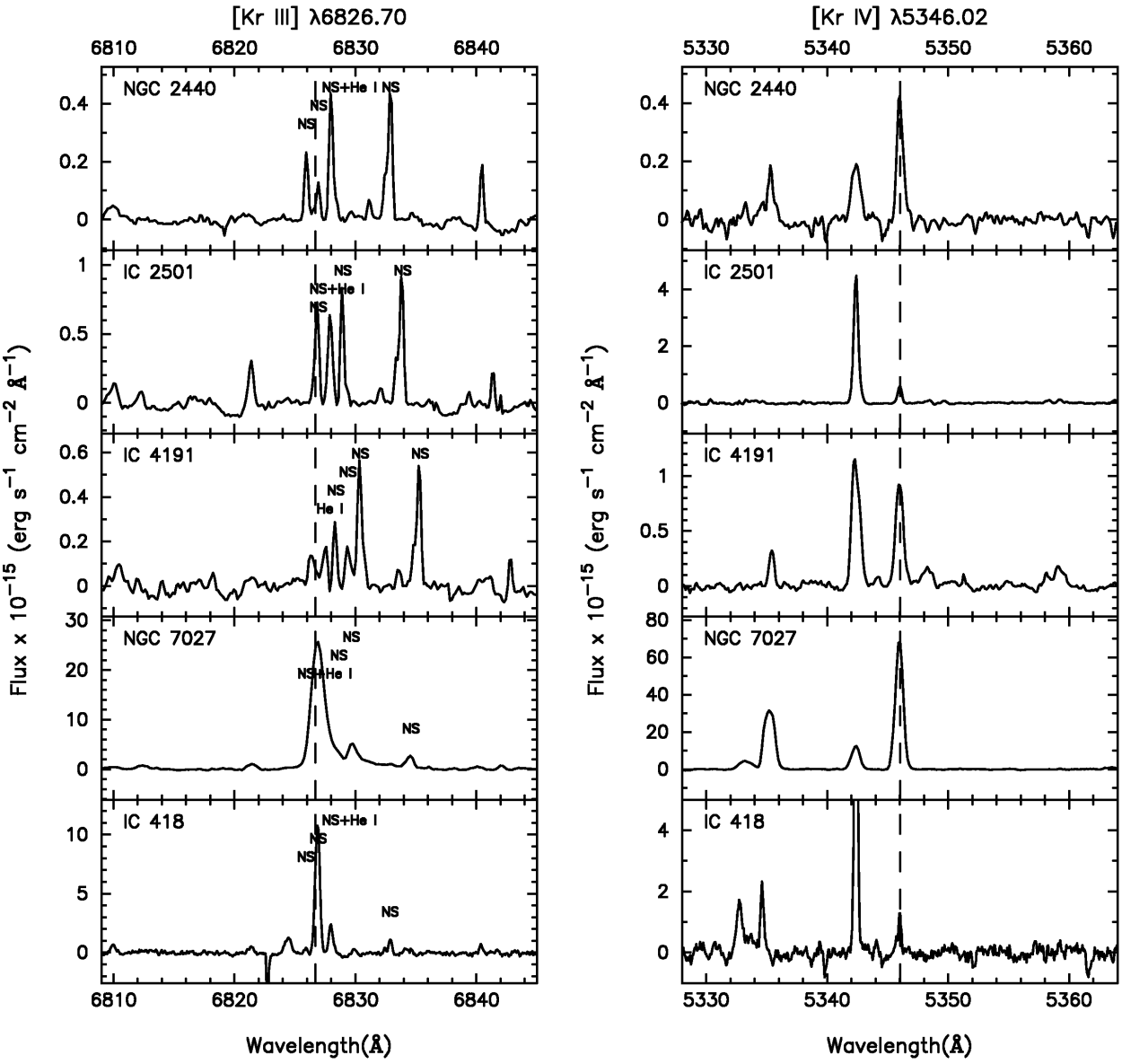

Fig. 4.— Continuum subtracted spectra in the immediate vicinity of several prominent Kr, Xe, and Br lines, shifted to each nebula's rest frame. Predicted wavelengths are indicated by dashed lines. Labels "NS" indicate telluric nightglow lines mentioned in the text. The regions around [Kr III] λ6826.70, [Kr V] λ6256.06, and [Xe III] λ5846.77 are expanded in subsequent figures and discussed in the text.

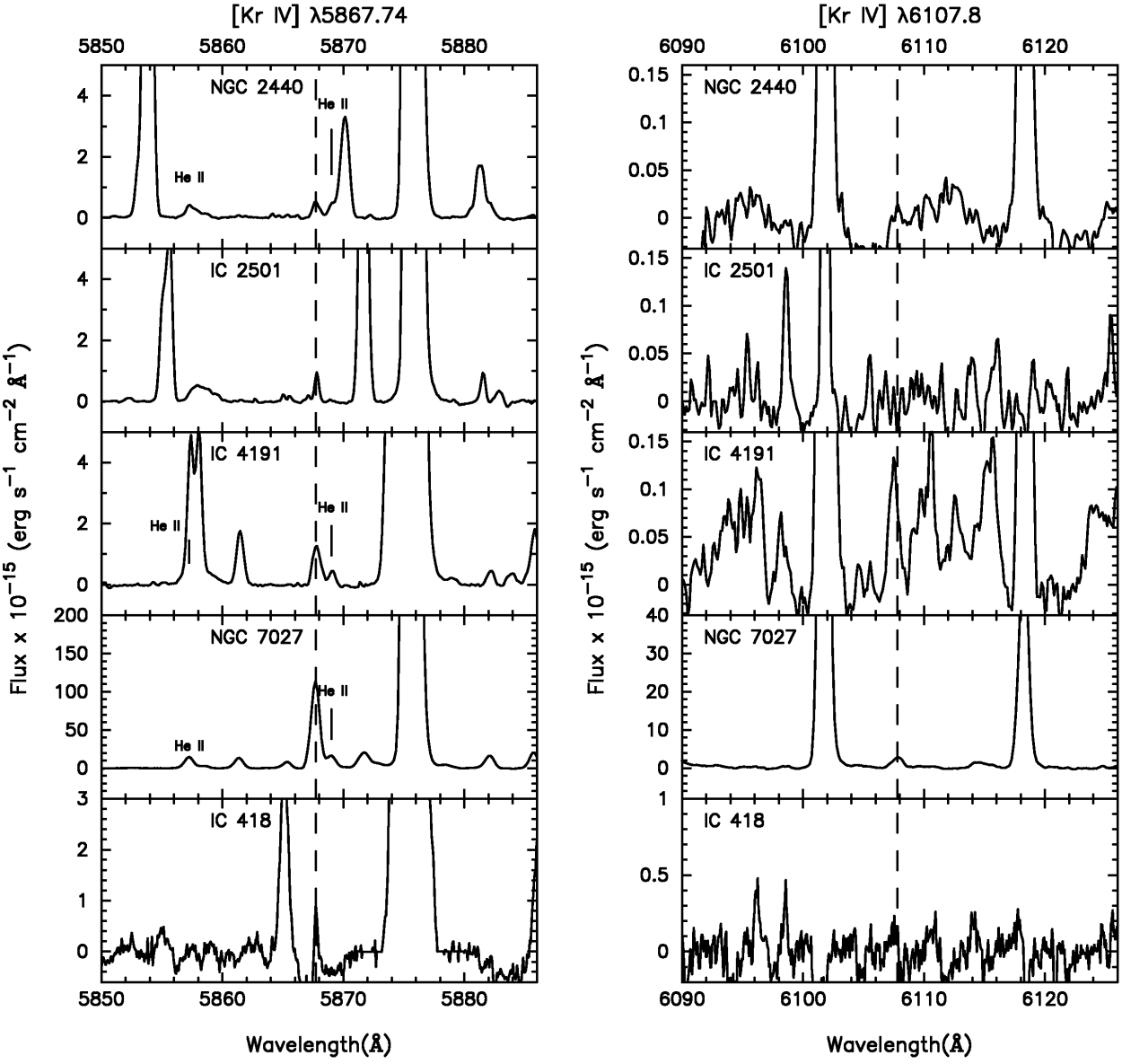

Fig. 4. — Continued.

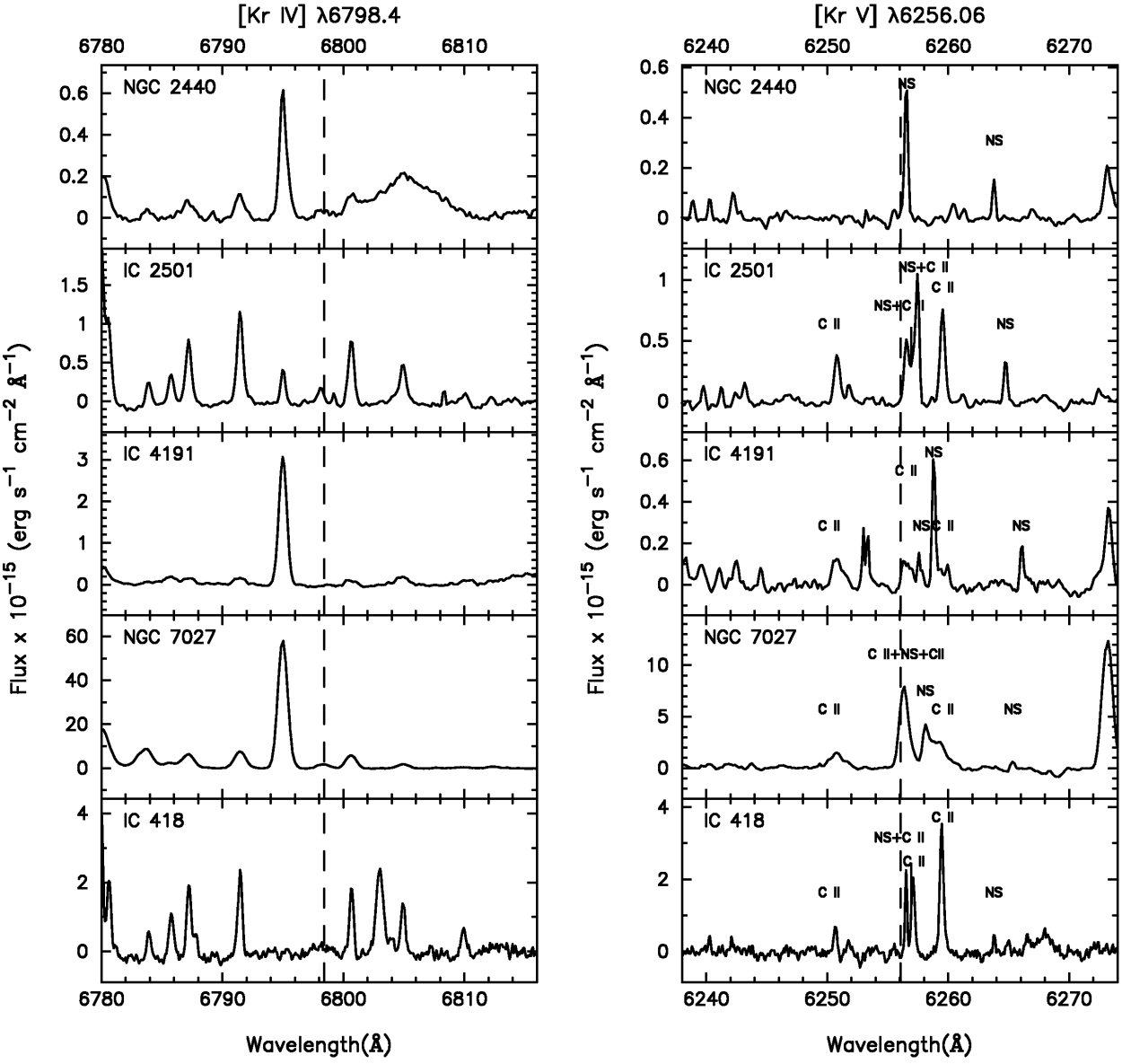

Fig. 4. — Continued.

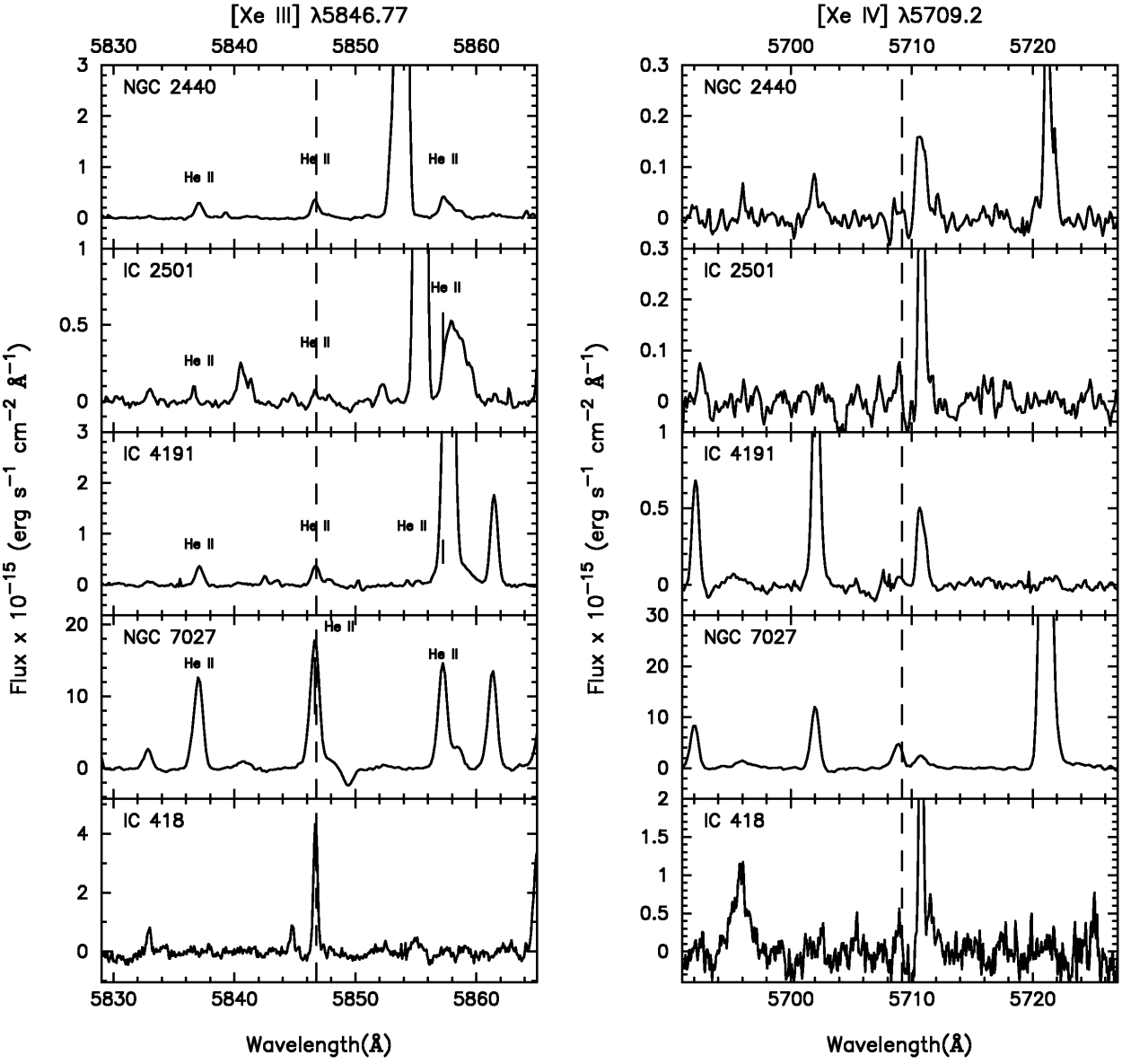

Fig. 4. — Continued.

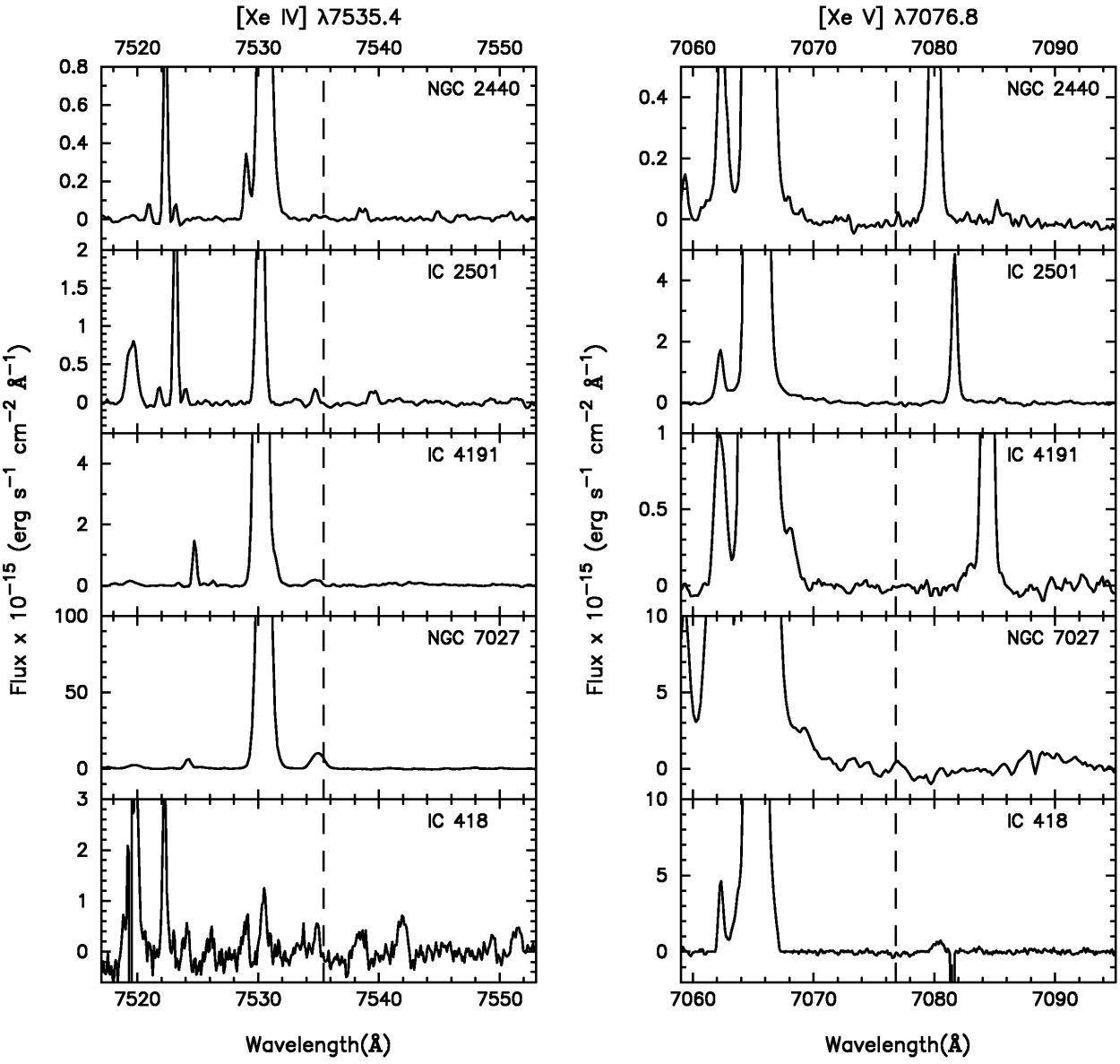

Fig. 4. — Continued.

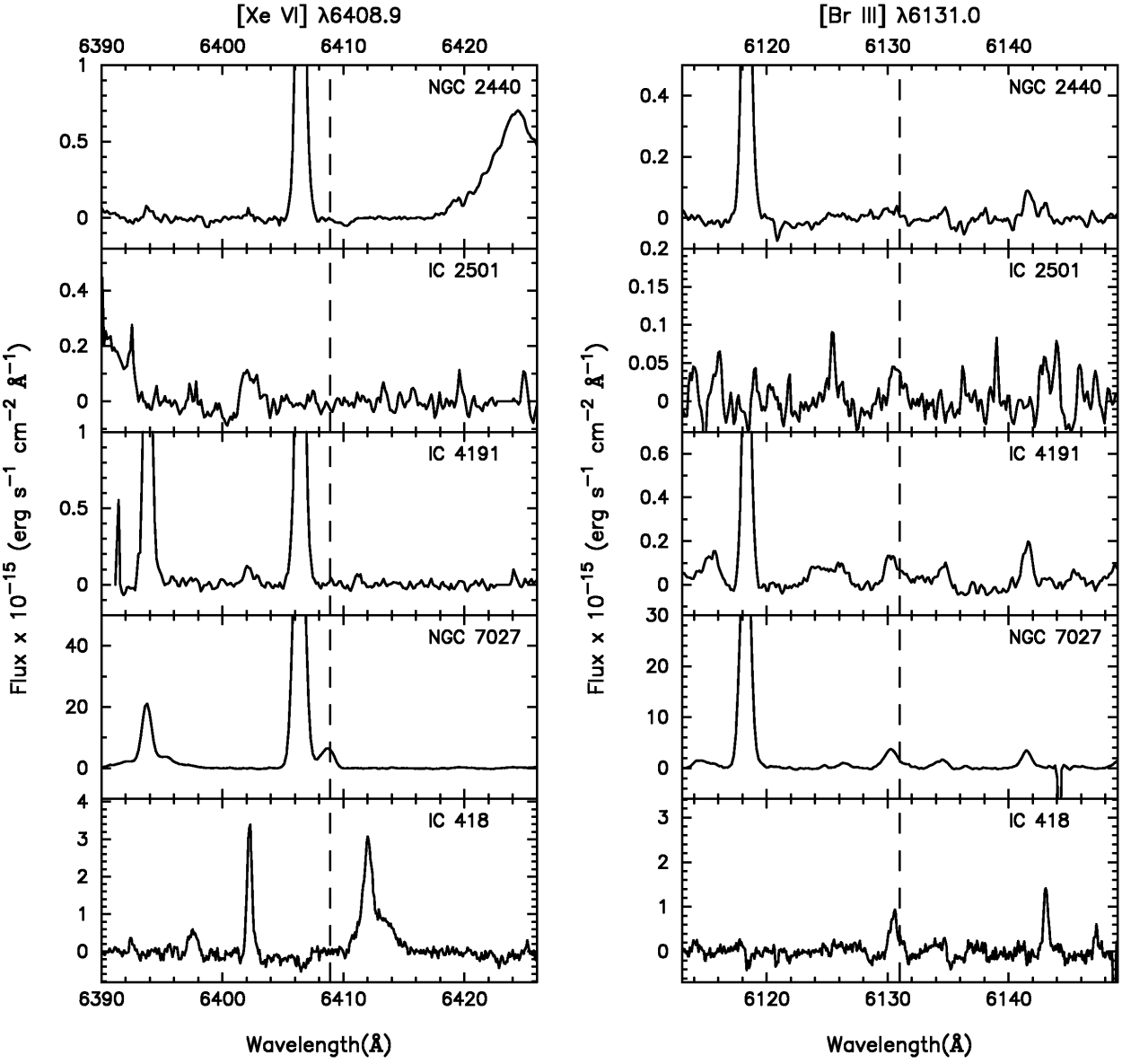

Fig. 4. — Continued.

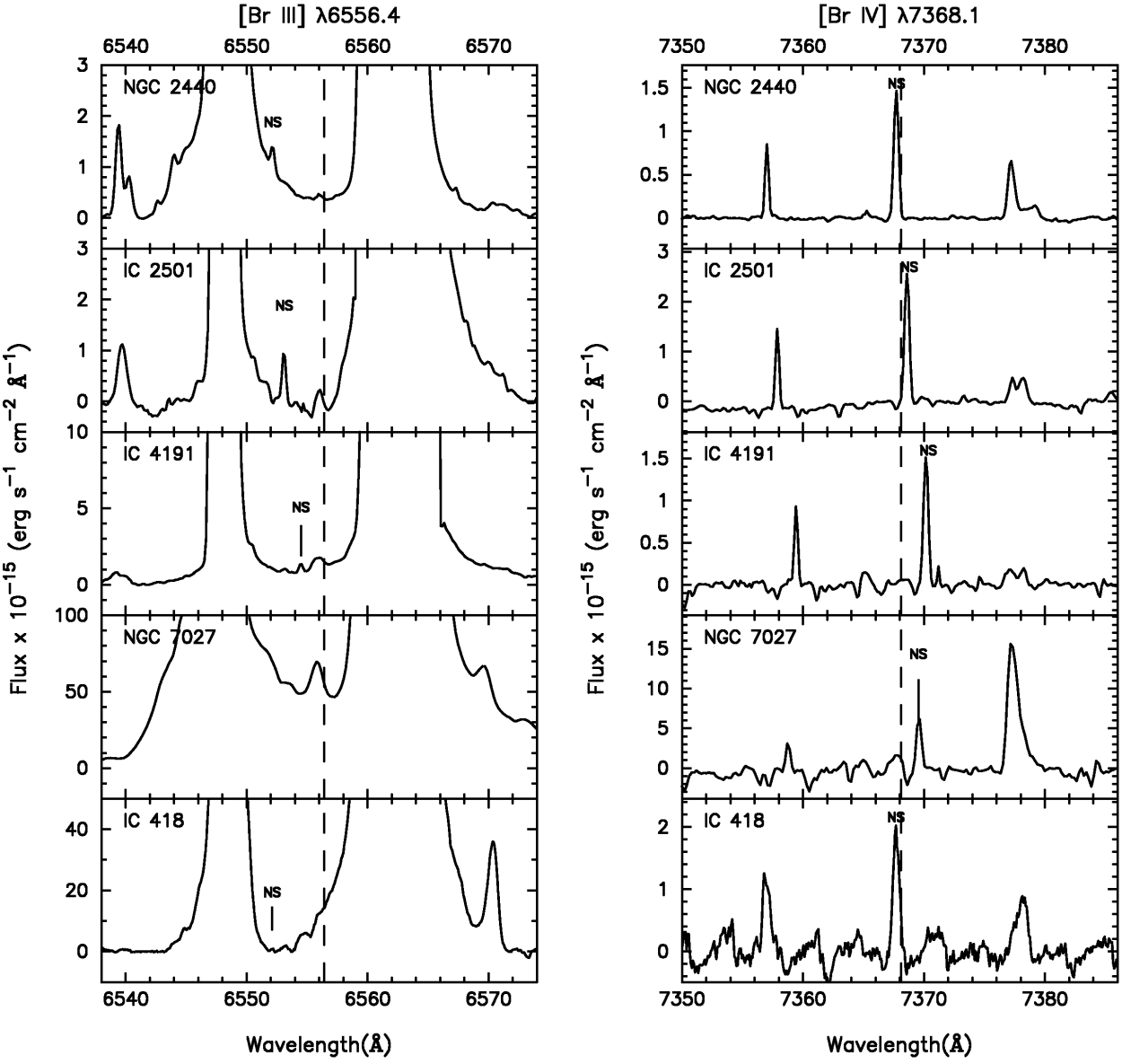

Fig. 4. — Continued.

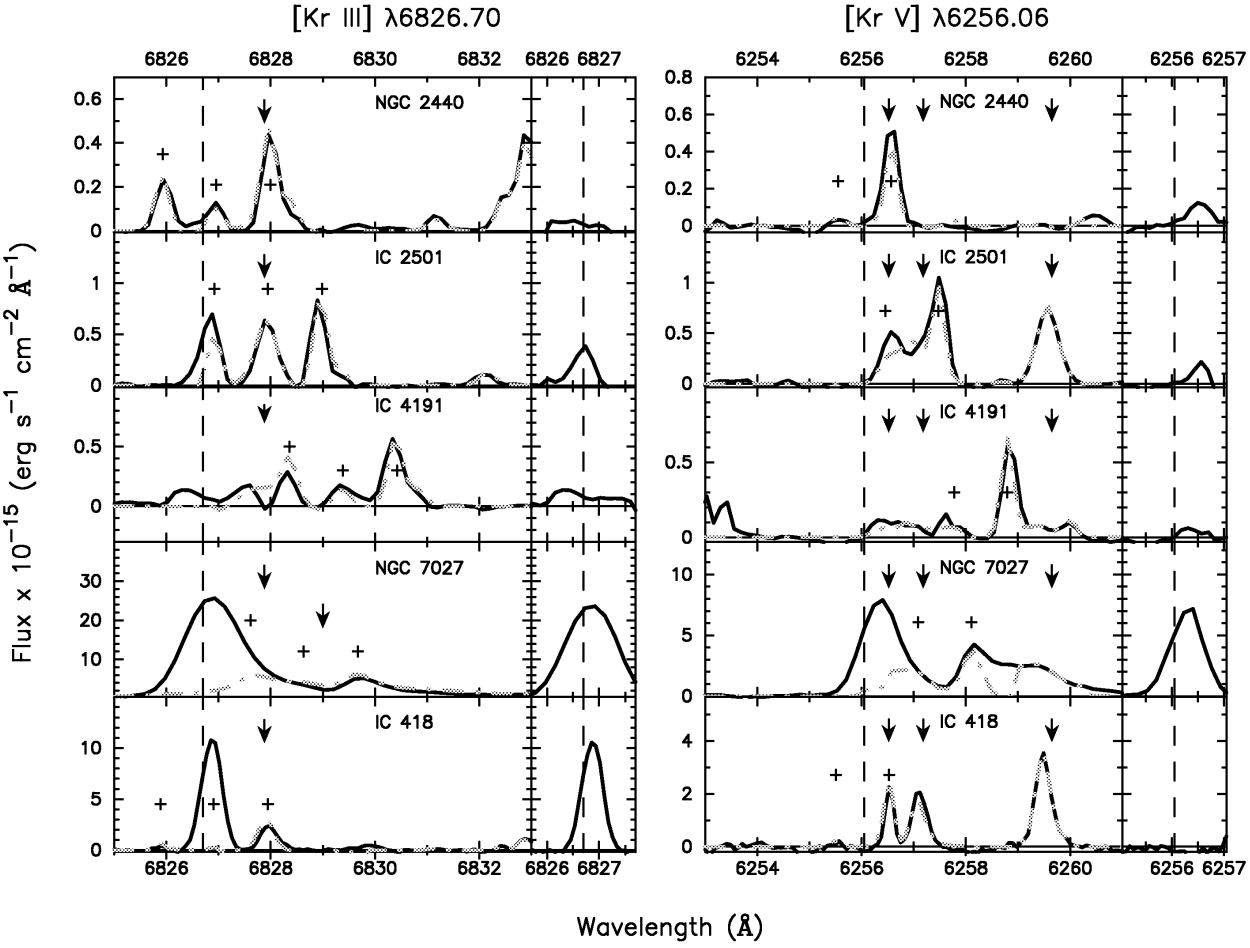

Fig. 5.— LEFT: Spectra in the vicinity of [Kr III] λ6826.70 (black line) shifted to nebular rest wavelengths, with similarly shifted and superimposed coadded modeled spectra of telluric emission and observed interloping nebular features (dot-dashed gray line). Pluses indicate telluric OH Meinel 7-2 $R_1(3.5)$ λ6827.46, $R_1(4.5)$ λ6828.47, and $R_1(2.5)$ λ6829.49 lines (left to right), nebular He I λ6827.88 is marked with an arrow, and a O VI λ1032 Raman feature at λ6829.16 (NGC 7027) marked with a lower arrow. RIGHT: Same for [Kr V] λ6256.06, with OH Meinel 9-3 $Q_2(0.5)$ λ6256.94 and $Q_1(1.5)$ λ6257.96 marked as pluses (left to right), and nebular C II λ6256.52, λ6257.18, λ6259.65 lines marked with arrows (left to right). Panels to right show residuals after subtraction in vicinity of predicted wavelengths of target line (vertical dashed line in all panels).

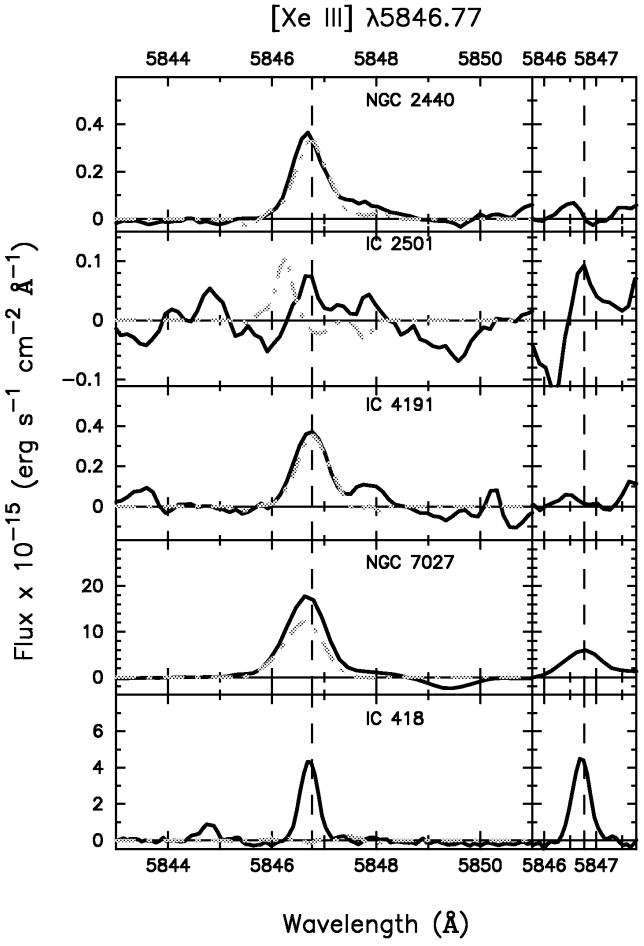

Fig. 6.— Spectra in vicinity of [Xe III] λ5846.77 (black line) shifted to nebular rest wavelengths, with superimposed profile of the He II 5-32 λ5837.06 shifted to the rest wavelength of the He II 5-31 line and scaled as described in the text (gray dot-dashed line). Panels to right show residual spectra after subtraction near the rest wavelength of the [Xe III] λ5846.77 line (vertical dashed line in all panels).